Catalysis Science & Technology

ROYAL SOCIETY OF CHEMISTRY

PERSPECTIVE

View Article Online
View Journal | View Issue

Cite this: *Catal. Sci. Technol.*, 2023, **13**, 3740

Copper-based metal–organic frameworks for CO_2 reduction: selectivity trends, design paradigms, and perspectives†

Ugochukwu Nwosu and Samira Siahrostami *

Can the carbon budget be balanced? Increasing greenhouse gas emissions and worsening environmental effects demand that humankind find a solution for anthropogenic climate change. As a carbon recycling strategy, the electrochemical carbon dioxide reduction reaction (CO_2RR) represents a platform to convert CO_2 to valuable chemicals. Despite the discovery that copper uniquely produces hydrocarbons, a lack of suitable catalysts prevents the realization of industrial-scale applications. Recently, metal–organic frameworks (MOFs), extended networks of organic ligands and metal nodes or clusters, have found application as electrocatalysts. Perhaps, this class of materials can be leveraged to tune the properties of copper and yield a suitable CO_2RR catalyst. In this review, we present new developments in the application of copper-based MOFs (Cu MOFs) for CO_2RR. Firstly, we highlight the potential of CO_2RR as a solution for carbon neutrality and proceed by overviewing CO_2RR mechanisms and catalysts. We then emphasize the role of copper which leads to our discussion of the trends in Cu MOFs for CO_2RR. We conclude by presenting several challenges and perspectives relevant to Cu MOFs in the hope of spurring targeted research in the field.

Received 26th March 2023,
Accepted 22nd May 2023

DOI: 10.1039/d3cy00408b

rsc.li/catalysis

1. Introduction

In lockstep with increasing atmospheric greenhouse gas levels, the pressure to advance CO_2 utilization technologies continues to rise. Research on CO_2 recycling *via* the electrochemical CO_2 reduction reaction (CO_2RR) has grown accordingly. As the sole pure metal electrocatalyst capable of producing valuable fuels and chemicals from CO_2, copper features extensively in CO_2RR research. In parallel, metal–organic frameworks (MOFs), extended networks of metal-containing nodes and organic ligands, have emerged as a class of materials with novel catalytic properties. Although numerous reviews exist on either the use of copper[1–10] or MOFs for CO_2RR,[11–17] to the best of our knowledge, no such reviews exist focusing solely on the use of copper-based MOFs (Cu MOFs) for CO_2RR. Herein, we aim to provide a critical review of the trends in this rapid developing field. Firstly, we motivate CO_2RR as a CO_2 recycling platform. We then describe CO_2RR mechanisms on copper, summarize electrocatalysts used for CO_2RR, and highlight the importance of copper. What follows is a critical analysis and summary of the developing trends regarding Cu MOFs used for CO_2RR. Finally, we conclude by presenting challenges and perspectives for CO_2RR on Cu MOFs.

2. CO_2 reduction for carbon neutrality

Owing largely to global energy and chemicals production, anthropogenic greenhouse gas (GHG) emissions constitute the vast majority of all GHG emissions on Earth.[18] Fig. 1 illustrates the global carbon cycle, highlighting the role of anthropogenic activities. In the decade beginning in 2012, fossil CO_2 emissions and emissions from land-use change averaged an estimated 10.8 gigatons of carbon per year (GtC per year). These emissions resulted in rising atmospheric CO_2 concentrations, 5.2 GtC per year, and uptake by ocean and terrestrial sinks, 2.9 GtC per year and 3.1 GtC per year, respectively.[18] Assuming 2022 emissions levels, the remaining carbon budget for a 50% likelihood to limit global warming to 1.5 °C is estimated to last for nine years.[18] As global warming is linked to a cascading list of environmental and socioeconomic problems,[18] balancing the carbon budget – *closing the carbon cycle* – is of global concern. This is underscored by the widespread ratification of the 2015 Paris Agreement. As of the date of writing this paper, 195 members of the United Nations Framework Convention on Climate

Department of Chemistry, University of Calgary, Calgary, Alberta T2N 1N4, Canada. E-mail: samira.siahrostami@ucalgary.ca

† Electronic supplementary information (ESI) available: The ESI includes tabulated reaction and property data for all of the metal–organic frameworks discussed in the main text as well as a description of the methodology used to compile data. The ESI file contains all the raw data for the tables in the ESI as well as additional experimental details for each study. See DOI: **https://doi.org/10.1039/d3cy00408b**

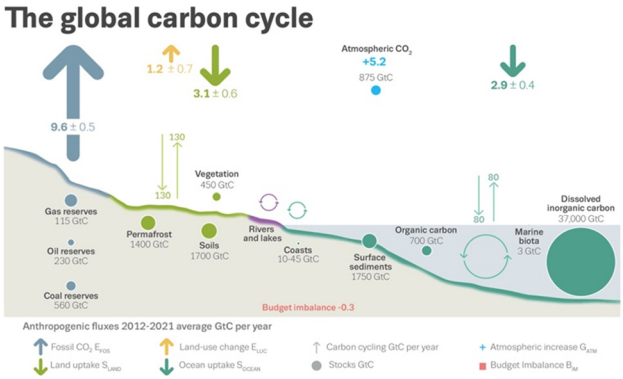

Fig. 1 Schematic representation of the global carbon cycle, highlighting effects from anthropogenic activities averaged globally for the decade 2012–2021. Arrows designate flows. Circles designate reserves. Cyclic arrows designate cycles. Quantities are specified in gigatons of carbon (GtC). The budget imbalance is a measure of imperfect data and understanding of the contemporary carbon cycle. All uncertainties are reported as one standard deviation. Reproduced from Friedlingstein *et al.*[18]

Change – all but three – have formally committed to reaching carbon neutrality by the year 2050.[19]

As one of three strategies of closing the carbon cycle, in addition to decarbonization and carbon sequestration, CO_2 recycling represents an important area of research requiring development. With the continued maturation and adoption of renewable energy, the attraction of CO_2RR as a CO_2 recycling platform has grown concomitantly. When powered by renewable energy sources, the mitigation of GHGs by CO_2-RR is two-fold. Firstly, carbon dioxide is converted to valuable chemicals and fuels, such as organic acids (*e.g.*, formic acid, acetic acid), alcohols (*e.g.*, methanol, ethanol), and/or hydrocarbons (*e.g.*, methane, ethylene). Secondly, the use of renewable energy foregoes the GHG emissions that would otherwise be emitted while producing valuable chemicals by existing carbon-intensive technologies. Furthermore, since oxidized carbon constitutes more than 70% of anthropogenic GHG emissions,[20] the chemical reduction of carbon sources represents an opposite solution. As vividly put by Nitopi *et al.*, "carbon reduction is as of yet a missing piece of humanity's industrial metabolism".[5]

3. CO_2 reduction reaction (CO_2RR) mechanisms

A great number of carbon products are possible from CO_2RR. This variety is simultaneously an advantage, as it widens the range of potential CO_2RR applications, and a disadvantage, as it hinders selectivity. An understanding of the mechanisms from which potential products arise is essential to navigating this duality to develop efficient catalysts. This section describes the potential chemical products from CO_2RR as well as key insights into their reaction mechanisms. We prioritize insights relevant to copper due to the theme of the present review.

3.1. CO_2RR products

Table 1 lists reduction potentials for CO_2RR as calculated by Nitopi and co-workers.[5] The potentials are calculated from the Gibbs free energy of reaction using gas-phase thermochemistry and Henry's Law data (for aqueous species) from NIST.[21]

The data in Table 1 highlights the inherent thermodynamic challenge to achieving selectivity in CO_2RR. Formic acid and carbon monoxide have been identified as economically viable targets.[22] The production of chemicals with two or more carbons (C_{2+} products) makes CO_2RR especially attractive for fuel production.[23] Yet, observe that the reduction potentials for all 14 products lie between −0.47 to 0.21 V and that five of the C_{2+} products listed exhibit reduction potentials in a 0.08 V range.

The reduction potentials do not tell the whole story, however. While thermodynamically, ethanol production should occur before hydrogen evolution, experimentally, hydrogen is typically the first reduction product observed. The experimentally observed kinetics can be related to the minimum energy path (MEP) for a given reaction mechanism. Specifically, the activation energies and free energy differences between intermediates along the MEP are relevant. In accordance with transition state theory and the computational hydrogen electrode model, large activation energies and free energy differences between reaction intermediates correlate with poor activities and prohibitive overpotentials.[24,25] Determination of complete reaction mechanisms as well as the rate-limiting and potential-determining steps requires performing both computational studies and *in situ*/*operando* experimental measurements.

3.2. Key sub-pathways in CO_2RR

It is important to note that CO_2RR mechanisms are by no means concretized as much debate and work continues in the field. CO_2RR mechanisms vary depending on the catalyst as well as the reaction conditions. Our aim here is not to give a definitive account of CO_2RR mechanisms but to highlight important intermediates and reaction steps for CO_2RR. Accordingly, we illustrate three sub-pathways (Fig. 2). The sub-pathways chosen feature frequently in reported reaction mechanisms and are relevant to alcohol and hydrocarbon formation. For a more extensive summary of CO_2RR mechanisms, we direct the reader to Section 5 of the review by Nitopi and co-workers.[5]

The first sub-pathway pertains to the formation of two-electron products CO and HCOOH (Fig. 2a). Fig. 2a shows the mechanism for producing HCOOH. CO_2 undergoes a proton-coupled electron transfer (PCET) to yield an *OCHO intermediate bound to the surface by two oxygen atoms. *OCHO is further reduced to HCOOH. Alternatively, the PCET can yield a *COOH intermediate which is further reduced to CO. In general, surface-bound oxygen species are common to the proposed mechanisms for HCOOH production while surface-bound carbon species are common to the proposed

Table 1 Electrochemical reactions with reduction potentials (298 K, 1 atm). Reproduced with permission from Nitopi *et al.*[5] Copyright 2019 American Chemical Society

Reaction	E^0/[*V vs.* RHE]	Product/reaction name
$2H^+ + 2e^- \rightarrow H_{2(g)}$	0	Hydrogen evolution reaction (HER)
$2CO_2 + 2H^+ + 2e^- \rightarrow (COOH)_{2(s)}$	−0.47	Oxalic acid
$CO_2 + 2H^+ + 2e^- \rightarrow CO_{(g)} + 2H_2O_{(l)}$	−0.10	Carbon monoxide
$CO_2 + 2H^+ + 2e^- \rightarrow HCOOH_{(aq)}$	−0.12	Formic acid
$CO_2 + 4H^+ + 4e^- \rightarrow C_{(s)} + 2H_2O_{(l)}$	0.21	Graphite
$CO_2 + 6H^+ + 6e^- \rightarrow CH_3OH_{(aq)} + H_2O_{(l)}$	0.03	Methanol
$CO_2 + 8H^+ + 8e^- \rightarrow CH_{4(g)} + 2H_2O_{(l)}$	0.17	Methane
$2CO_2 + 8H^+ + 8e^- \rightarrow CH_3COOH_{(aq)} + 2H_2O_{(l)}$	0.11	Acetic acid
$2CO_2 + 10H^+ + 10e^- \rightarrow CH_3CHO_{(aq)}$	0.06	Acetaldehyde
$2CO_2 + 12H^+ + 12e^- \rightarrow C_2H_{4(g)} + 4H_2O_{(l)}$	0.08	Ethylene
$2CO_2 + 12H^+ + 12e^- \rightarrow C_2H_5OH_{(aq)} + 3H_2O_{(l)}$	0.09	Ethanol
$2CO_2 + 14H^+ + 14e^- \rightarrow C_2H_{6(g)} + 4H_2O_{(l)}$	0.14	Ethane
$3CO_2 + 16H^+ + 16e^- \rightarrow C_2H_5CHO_{(aq)} + 5H_2O_{(l)}$	0.09	Propionaldehyde
$3CO_2 + 18H^+ + 18e^- \rightarrow C_3H_7OH_{(aq)} + 5H_2O_{(l)}$	0.10	1-Propanol

mechanisms for CO. Although DFT calculations suggest that *COOH formation may thermodynamically limit CO production,[26] recent theoretical and experimental results suggest that CO_2 adsorption is the rate-limiting step for both CO and HCOOH formation on a range of transition metals.[27]

The second sub-pathway goes through protonation of the *CO intermediate (Fig. 2b). *CO is ubiquitous in CO_2RR as it has been reported as an intermediate in the proposed mechanisms for all CO_2RR products but formate.[5] Both experimental and theoretical studies indicate that hydrocarbon production on copper proceeds through a *CO intermediate.[26,28–31] Protonation of the oxygen atom yields a *COH intermediate while protonation of the carbon atom yields a *CHO intermediate.[32,33]

Reports indicate that on copper surfaces, the set of favoured C_1 products from the *COH and *CHO intermediates differ.[33–36] For example, Nie *et al.* reported that on the Cu(111) surface, formation of *CHO favours methane production while the formation of *COH favours methane, methanol, and ethylene production.[37] This implies that *CO protonation is a selectivity-determining step.[33–36] Thus, stabilization of the subsequent protonated intermediate can enhance the selectivity of particular CO_2RR products. Analogously, stabilization of the transition state of the rate-limiting step can improve CO_2RR kinetics. However, as identification of the transition state can be challenging, DFT calculations can provide correlations for the activation energy.

For example, Liu *et al.* obtained linear scaling relations correlating the free energy of the *CO → *CHO transition state complex (H–CO*) with the adsorption energy of *CO (Fig. 3a) and *CHO (Fig. 3b) on (211) and (111) metal surfaces.[33] Peterson and Nørskov obtained similar relations for the adsorption energy of carbon-bound intermediates (*COOH, *CHO, and *CH_2O) *vs.* *CO (Fig. 3c) and oxygen-bound intermediates (*O and *OCH_3) *vs.* *OH (Fig. 3d) on fcc(211) metal surfaces.[26] Such relations suggest activity descriptors for ideal catalysts – for instance, CO adsorption energy for CH_4 and C_{2+} production.[26,38]

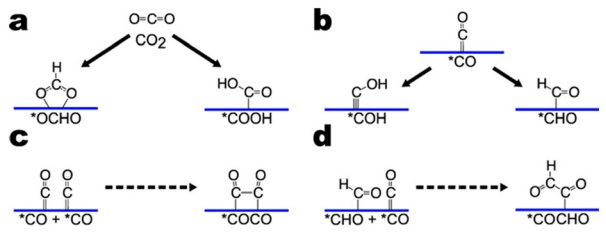

Fig. 2 Selected sub-pathways of CO_2RR. a) Proton-coupled electron transfer of CO_2 to *OCHO or *COOH. b) Proton-coupled electron transfer of *CO to *COH or *CHO. c) *CO dimerization reaction. d) C–C coupling of *CHO and *CO. Solid lines denote proton-coupled electron transfers. Dashed arrows denote coupling reactions.

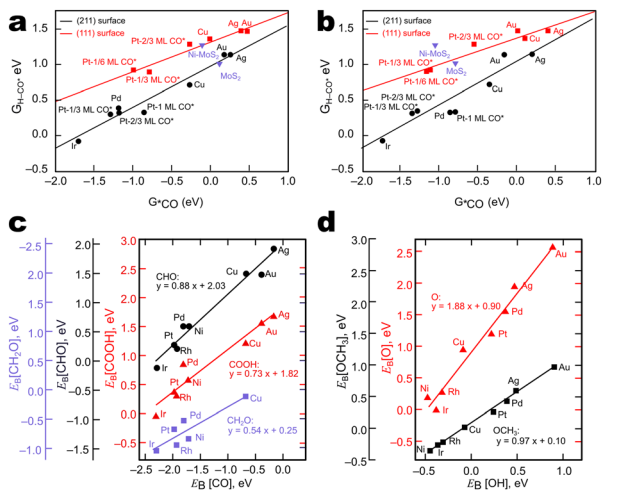

Fig. 3 Linear scaling relations between the adsorption energies of important CO_2RR intermediates on transition metal (211) and (111) surfaces a) G_{H-CO*} *vs.* G_{*CO}. b) G_{H-CO*} *vs.* G_{*CHO}. Adapted with permission from Liu *et al.*[33] Copyright 2017 Nature Publishing. Linear scaling relations between the adsorption energies of important CO_2RR intermediates on transition metal FCC(221) surfaces. c) E_B [CH_2O], [CHO], [COOH] *vs.* E_B [CO] d) E_B [OCH_3] and [O] *vs.* E_B [OH]. Adapted with permission from Peterson & Nørskov.[26] Copyright 2012 American Chemical Society.

The third sub-pathway pertains to C–C coupling. Numerous C–C coupling mechanisms are feasible depending on the nature of the catalyst employed. On catalysts with adjacent active sites, C–C coupling may occur through direct coupling of adsorbed intermediates, potentially mediated by an electron transfer.[39] Alternatively, gaseous CO may react with adsorbed species to form similar intermediates. Fig. 2c and d illustrate two frequently reported C–C coupling mechanisms, CO dimerization and CO–CHO coupling.

Although the C–C coupling steps are not typically potential-determining, the observed pH dependence of C_{2+} yields suggests that the C–C coupling may be rate-determining on Cu.[29,40–43] Kinetic barriers of C–C coupling steps that are not mediated by an electron transfer differ from PCET steps in that their energetics are not influenced in the same way by the chemical potential of aqueous protons. Field effects and solvent stabilization primarily influence the kinetic barriers of C–C coupling steps.[40,44,45] DFT calculations on the Cu(211) surface indicate that C–C coupling proceeds more favourably for further hydrogenated intermediates.[44] However, calculations on the Cu(211), Cu(111), and Cu(100) surfaces also support the feasibility of CO dimerization.[39,40,45,46]

Finally, it is important to note that the energetics of *OH and *H adsorption are also relevant for CO_2RR performance. Strong OH binding can result in catalyst poisoning while *H adsorption dictates the kinetics of the hydrogen evolution reaction (HER). An ideal catalyst must suppress these side reactions yet still exhibit reasonable CO_2RR kinetics at a low overpotential. The next section will discuss previous attempts to find such a material.

4. CO_2RR catalysts

Broadly, CO_2RR electrocatalysts can be classified as either homogeneous[47] or heterogeneous,[11] and they can be further categorized as metal or nonmetal catalysts. Nonmetal-doped carbon allotropes constitute the majority of nonmetal catalysts studied for the CO_2RR. The presence of heteroatoms, such as boron, nitrogen, and sulfur, is required to endow carbon materials (graphene, carbon nanotubes (CNTs), and porous carbon) with CO_2RR activity.[48–50] Metal-containing CO_2RR catalysts include pure transition metal catalysts[51,52] as well as metal-doped carbon,[49,50,53,54] metal oxides/nitrides and alloys,[35,55–57] and organic–inorganic hybrid materials.[41,52,55,58] Fig. 4 illustrates the various categories of electrocatalysts employed for CO_2RR. For a comprehensive overview of CO_2RR catalysts, the reader is encouraged to consult other reviews and perspectives.[5,6,9,59–64]

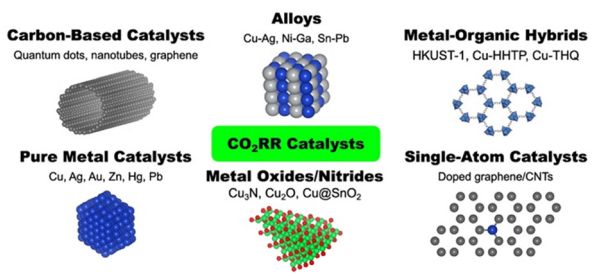

Fig. 4 Various types of CO_2RR catalysts.

Although metal-free carbon-based catalysts have shown great promise due to their favourable physical and electrical properties, experimental and theoretical investigations indicate that in order to reduce CO_2 further than CO, the presence of a metal component is necessary.[53] Of note, single atom catalysts (SACs), which contain isolated metal atoms, have been investigated for the CO_2RR.[53,54,65–67] The enhanced catalytic performance of SACs compared to bulk metal catalysts derives from the undercoordination of metal atoms in open metal sites (OMSs).[54] The isolated catalytic sites offer fine-tuned control over the electronic structure of the metal. SACs also exhibit superior metal utilization compared to both bulk and nanoparticle catalysts due to the maximal dispersion of metal atoms in SACs.

Importantly, the choice of metal directly affects the CO_2-RR product such that metals can be separated into four groups based on their tendency to form CO_2RR products. Formate-producing metals include Pb, Hg, Tl, In, Sn, Cd, and Bi; carbon monoxide-producing metals include Au, Ag, Zn, Pd, and Ga. Ni, Fe, Pt, and Ti display minimal activity for CO_2 reduction. Copper is unique in that it is the only pure metal capable of producing C_{2+} products.[5,41] This essential property makes copper the subject of immense interest for the CO_2RR.

5. The importance of copper

5.1. The origin and challenge of C_{2+} selectivity

As previously mentioned, copper uniquely produces a variety of hydrocarbon and oxygenated products.[30,41,68–72] From a thermodynamic standpoint, the trends in CO_2RR activity among transition metals may be explained by the binding energies of *CO and *H. Fig. 5 illustrates the unique adsorption properties of copper relative to other transition metals.

Using a two-parameter descriptor, Hussain *et al.* classified the electrocatalytic activity of various transition metal electrodes.[73] Observe that copper is the sole metal lying within the H_2/hydrocarbons and alcohols region. Copper exhibits an intermediate binding energy for CO and a positive binding energy for *H.[34] In accordance with the Sabatier principle,[74] the intermediate *CO binding energy on copper balances CO poisoning and activation, resulting in the ability to yield products of reductions of more than two electrons ($>2e^-$ products). The positive binding energy for *H explains copper's preference for CO_2RR over HER.[26,34,38,73,75]

The unique ability of copper to produce $>2e^-$ products is unfortunately also a pitfall as copper can produce up to 14 different products (Table 1).[76] This wide range of potential products augments the challenge of selectivity of copper catalysts.

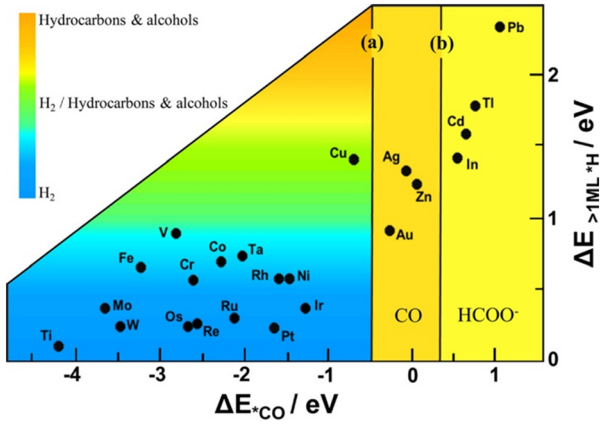

Fig. 5 Two-parameter descriptor of the electrocatalytic activity of metal electrodes. The relative rate of CO_2 reduction and H_2 formation is shown as a function of the binding energy of an isolated CO molecule (horizontal axis) and differential adsorption energy of an H-adatom at an on-top site (vertical axis), occupied once the coverage exceeds one monolayer. Lines (a) and (b) demarcate the transition between CO poisoning/desorption and CO/$HCOO^-$ desorption. Reproduced with permission from Hussain *et al.*[73] Copyright 2018 American Chemical Society.

5.2. Relevant strategies for improving the CO_2RR performance of copper

Various strategies have been examined to improve the selectivity and activity of copper for CO_2RR. Herein, we highlight trends in CO_2RR performance on copper catalysts with counterparts in the field of copper-based MOFs to be discussed in the next section. Namely, we note trends involving the copper coordination environment and synergistic effects with non-copper atoms. Although there are additional factors affecting copper CO_2RR performance, such as the oxidation state and electrolyte, we defer to existing reviews as discussion of these factors is beyond the scope of this review.[5,77] However, investigation of these effects as they relate to copper-based MOFs would be beneficial to the field.

5.2.1. Tuning the copper coordination environment. The importance of the copper coordination environment is evidenced by the facet dependence of CO_2RR on copper. Single-crystal studies report that the different facets of copper exhibit distinct CO_2RR performances.[57,69–71,78,79] Additionally, theoretical studies reveal that the mechanism of C–C coupling differs between copper facets.[36,39,40,44,45] Microkinetic models of CO reduction on copper surfaces suggest that despite comprising a small fraction of sites, the low-coordination copper atoms on stepped surfaces contribute predominantly to the overall activity.[33]

Since the coordination of surface atoms is a principal difference between copper facets, the coordination number has been suggested as a key descriptor for catalytic performance. Indeed, that the generalized coordination number (GCN) proposed by Calle-Vallejo *et al.* correlates with catalytic performance underscores the relationship between site coordination and catalytic performance.[80] However, although manipulation of the crystal facet can enhance selectivity for C_{2+} products, the use of single crystals as electrocatalysts is impractical due to their low geometric surface area and resulting low current densities.[5] Nonetheless, the link between coordination and C_{2+} selectivity motivates the development of copper catalysts with undercoordinated sites by different means.

Nanostructured and single-atom catalysts attempt to leverage this phenomenon.[65,81] As particle size decreases, the number of undercoordinated surface atoms increases.[5] Additionally, the nature of single-atom catalysts can decouple adsorbate binding energies and unlock novel selectivity.[67] In light of this, studies suggest that copper nanoparticles and mesocrystals may lead to high C_{2+} faradaic efficiencies.[82] However, no clear connection between particle size and C_{2+} selectivity can be identified as studies indicate that peak hydrocarbon selectivity can be achieved at different particle sizes.[83–85] All of this serves to highlight the possibility that a different paradigm for altering copper coordination could better take advantage of the connection between coordination and selectivity.

5.2.2. Modification of copper catalysts by incorporation of heteroatoms. The CO_2RR performance of copper also depends on the presence of other atoms.[35,86] Combining copper with HCOOH-producing metals (In, Sn) generally results in HER suppression, $>2e^-$ product suppression, and synergistic CO production.[5] Combining copper with H_2- or CO-producing metals generally increases the selectivity of the corresponding product.[5,57,87–89] In some cases, however, combination of copper with a CO-producing metal results in a synergistic effect, boosting selectivity for $>2e^-$ products by CO spillover[90,91] or electronic effects.[92–94] Nonetheless, save for a few examples of tandem catalysis, the intrinsic activity of bimetallic systems generally fails to surpass that of copper for $>2e^-$ products.[5]

In terms of non-metal atoms, subsurface oxygen in oxide-derived copper can enhance *CO adsorption and promote H_2O adsorption and subsequent electron transfer between CO_2 and H_2O.[1,94,95] Boron doping increases the prevalence of catalytically active $Cu^{\delta+}$ species, increasing C_{2+} production.[89] Finally, the functionalization of copper surfaces with ligands or dopants can also serve to stabilize key intermediates and enhance CO_2RR performance.[89,96–99] Despite the advances in CO_2RR catalyst development, alcohol and hydrocarbon production still requires large overpotentials of up to 1 V and suffers from low selectivity.[2,30,76] Further, the reported increases in current density for functionalized copper surfaces do not correspond to increases in intrinsic activity – that is, activity normalized by electrochemical surface area.[100] Thus, the door is still open for increasing the CO_2RR performance of copper.

6. Copper-based metal–organic frameworks

Metal–organic frameworks (MOFs), also referred to as porous coordination polymers, are extended networks of metal nodes

or clusters bridged by simple organic ligands through metal–ligand coordination bonds.[101] A metal centre or inorganic cluster constitutes the secondary building unit (SBU). Note that we use the terms "node" and "cluster" to denote SBUs featuring single and multiple metal atoms, respectively. The SBUs can be tuned to change the structure, gas adsorption, catalytic ability, electrical conductivity, and porosity of the MOF. Additionally, the choice of ligand and other factors such as counterions, pH, temperature, and solvents can influence MOF properties.[102]

The two most widely used classes of ligands for MOF synthesis are N-donors and O-donors, composed primarily of pyridyl- and carboxylate-based ligands, respectively (Fig. 6). However, due to the requirement of strong metal–ligand bonds for retaining the structural integrity of MOFs after solvent removal, carboxylate ligands are more prevalent in MOF structures.[101] Further, both pyridyl- and carboxylate-based ligands are dominated by rigid phenyl- or ethynyl-containing molecules, which are fundamental for the directional bonding in MOFs.[101] It should be noted that although less studied, phosphonate and sulfonate ligands may also be used in MOFs.[102] For a comprehensive treatment of the structure and synthesis of MOFs, we refer the reader to other works.[101–105]

Recently, MOFs have gained popularity due to their novel properties. MOFs exhibit high porosity, large surface areas, unique host–guest dynamics, thermal stability, and mechanical flexibility.[102] In contrast to copper within pure metal surfaces, which primarily exists in the zero oxidation state, copper within MOFs also exists in the +1 and +2 oxidation states (Table S1†). Like SACs, MOFs feature isolated catalytic sites; however, their reticular nature enables more precise design of active sites than in SACs. Could metal–organic frameworks be the key to unlocking C_{2+} selectivity in copper catalysts? To this end, we limit the scope of our discussion to metal–organic frameworks featuring copper atoms within the secondary building unit, copper-based metal–organic frameworks (Cu MOFs). Specifically, our scope is limited to Cu MOFs reported as the catalytic material for CO_2RR.

Beginning with formate production by copper rubeanate in 2012 (ref. 106) and oxalic acid production by HKUST-1 in the same year,[107] copper-based metal–organic frameworks have been increasingly investigated for CO_2RR. Although the goal of this review is not to merely summarize recent results of Cu MOFs, we have compiled comprehensive property and CO_2RR performance data for Cu MOFs in the ESI† and the ESI† file for reference.

Herein, we reveal promising trends in Cu MOF design, assess proposed explanations for observed phenomena, and suggest promising new lines of inquiry regarding Cu MOFs for CO_2RR. We focus on the secondary building unit as a determinant of selectivity, the effect of the MOF ligand, and strategies for improving selectivity by the incorporation of other transition metals and nanocluster–MOF composites. Finally, we conclude with a discussion of the stability of Cu MOFs.

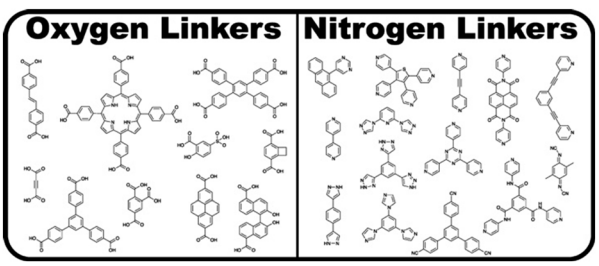

Fig. 6 MOF ligands featuring oxygen and nitrogen linkers. Adapted with permission from Cook *et al.*[101] Copyright 2013 American Chemical Society.

6.1. The dependence of C_{2+} selectivity on the secondary building unit

As was mentioned as a motivation for single-atom catalysts and nanoparticles, modification of the copper coordination environment may be the key to designing efficient CO_2RR catalysts. For bulk copper catalysts and SACs, there exists a great body of work presenting descriptors for CO_2RR performance.[53,108,109] In the spirit of said work, this section focuses on how the copper coordination environment in Cu MOFs relates to CO_2RR performance. Specifically, we discuss how the type, number, and geometry of atoms which coordinate copper within the SBU affect the selectivity of CO_2RR in Cu MOFs. For the present discussion, we will specify metal node SBUs by the constituting metal and the atoms bonded to the metal. Thus, a single copper atom coordinated by four oxygen atoms will be referred to as a CuO_4 node.

6.1.1. Node-based SBUs. The vast majority of Cu MOFs reported as CO_2RR catalysts feature copper in a square planar coordination geometry (ESI† file). For copper, coordination geometries with four ligands generally yield two open metal sites (OMSs).[110] Thus, this trend is consistent with the fact that one descriptor for catalytically reactive metal sites is the presence of OMSs. In solution, the axial coordination positions are occupied by labile solvent molecules that may be replaced by adsorbates under CO_2RR conditions.[110] Numerous Cu MOFs in which copper resides solely within square planar nodes show CO_2RR reactivity; however, such Cu MOFs tend not to yield $>2e^-$ products. Slight variations in the geometry appear to dramatically shift the product distribution. The following study regarding three Cu MOFs featuring O-linked copper nodes illustrates this observation.

Liu *et al.* evaluated the performance of Cu-DBC[111] and compared it to that of Cu-THQ[112] and Cu-HHTP[113] obtained from published data. Cu-DBC features square pyramidal CuO_5 nodes. The CuO_5 nodes are partially constituted by two dibenzo-[*g*,*p*]chrysene-2,3,6,7,10,11,14,15-octaol (DBC) ligands coordinating a copper atom. Additionally, an axially coordinating oxygen atom bridges each copper atom in the SBU to a single other copper atom in an adjacent sheet (Fig. 7d). The SBU of Cu-THQ consists of CuO_4 nodes formed by two tetrahydroxy-1,4-quinone (THQ) ligands coordinating

a square planar copper. Cu-HHTP also features square planar copper within CuO_4 nodes; however, two 2,3,6,7,10,11-hexahydroxytriphenylene ligands coordinate the copper node. The structures of all three Cu MOFs are shown in Fig. 7.

According to the Dewar–Chatt–Duncanson model, the electronic structure of copper in a square pyramidal geometry features higher energy d orbitals than that of copper in a square planar geometry.[114–116] This d orbital elevation may facilitate stronger interaction between Cu and CO *via* π-back-bonding, which is favourable for hydrogenation. Preliminary DFT calculations by Liu *et al.* showed that the adsorption energy of *CO on CuO_5 sites was more than fifty percent larger than on the CuO_4 sites (73.42 kJ mol^{-1} *vs.* 48.6 kJ mol^{-1}).[111]

Comparison of the CO_2RR performance of the three Cu MOFs revealed stark differences in selectivity. While Cu-HHTP and Cu-THQ exhibited exclusively CO production (42% FE_{CO} and 91% FE_{CO}, respectively), Cu-DBC exhibited 56% FE_{CH_4}.

DFT calculations explain the disparities in selectivity. The free energy diagram reveals that CO is more stable on the CuO_4 nodes than on the CuO_5 nodes relative to free CO (−0.23 eV *vs.* −0.18 eV) (Fig. 8). Notably, the difference in CH_4 production derives from the stability of the $*OCH_2$ intermediate relative to the preceding intermediate (*CHO). The free energy difference of this elementary step is 0.24 eV less on the CuO_5 node than on the CuO_4 node (0.35 eV *vs.* 0.59 eV, respectively).

We note, however, that the experimental conditions for the comparison between Cu-DBC, Cu-THQ, and Cu-HHTP were not uniform. First, the CO_2RR performance of Cu-THQ was tested in an alkaline choline chloride solution. Second, while the electrolytes used to test Cu-DBC and Cu-HHTP performance were the same (0.1 M $KHCO_3$), the experimental setups used to test CO_2RR performance differed, and the studies do not directly compare their results to benchmarks.

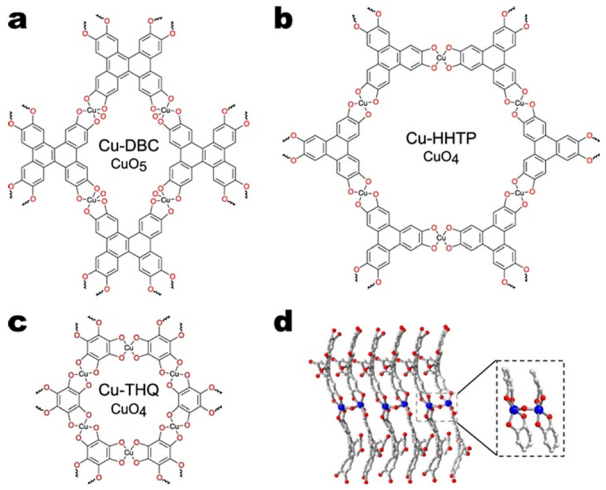

Fig. 7 Structures of a) Cu-DBC, b) Cu-HHTP, and c) Cu-THQ. d) Close-up of the CuO_5 node present in Cu-DBC. The blue, red, and white spheres denote copper, oxygen, and carbon atoms, respectively. Adapted with permission from Liu *et al.*[111] Copyright 2022 American Chemical Society.

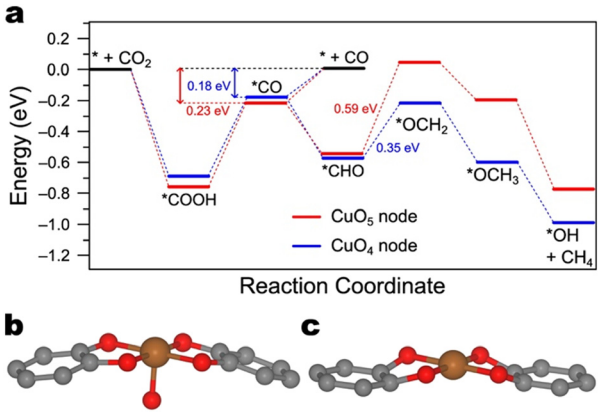

Fig. 8 a) Free energy diagram of CH_4 production on CuO_5 and CuO_4 nodes. Data from Liu *et al.*[111] The free energies of CO adsorption were inferred from the free energy differences between steps presented in the original publication. Illustration of the cluster models of b) CuO_5 and c) CuO_4 nodes employed for calculation of the free energy diagrams in Fig. 8a by Liu *et al.*[111] The orange, red, and grey spheres denote copper, oxygen, and carbon atoms, respectively.

For comparison, we note the work by Zhang *et al.*, which tested Cu-DBC and Cu-HHTP under alkaline conditions and reported CH_4 production by both Cu-DBC (80% FE_{CH_4} at −0.9 V *vs.* RHE) and Cu-HHTP (42.6% FE_{CH_4} at −0.9 V *vs.* RHE). C_2H_4 production by Cu-HHTP (40.9% $FE_{C_2H_4}$ at −0.8 V *vs.* RHE) was also reported.[117] These results challenge the notion that the CuO_5 node plays a definitive role in CH_4 production. Thus, an analogous study under neutrally buffered conditions would more definitively illustrate the role of the CuO_5 node. Nonetheless, the results by Liu *et al.* provide an important starting point for investigations of the effect of copper coordination geometry on CO_2RR performance.

When copper resides within square planar CuN_4 nodes, it appears that the copper sites either serve for CO production or are ineffective for CO_2RR altogether.[118] In fact, DFT calculations on various metallophthalocyanine-based Cu MOFs indicate that the free energy change for *COOH formation is consistently greater on CuN_4 nodes compared to the analogous CuO_4 nodes.[115] Fig. 9a and b indicate that for both sequential and concerted PCET mechanisms, *COOH formation proceeds more readily on PcCo–Cu–O and PcNi–Cu–O MOFs than on PcCo–Cu–NH and PcNi–Cu–NH MOFs, respectively. However, the work by Zhao and co-workers suggests that as edge sites, nitrogen-coordinated copper may be active for C_{2+} product formation. Cu-HITP, a structural analogue of Cu-HHTP featuring CuN_4 nodes, exhibited 62% $FE_{>2e^-}$ and 43% $FE_{C_{2+}}$ at −1.2 V *vs.* RHE. DFT calculations indicate an interplanar C–C coupling mechanism between *CO and *COH on adjacent edge sites.[119]

Cu MOFs featuring CuO_4 nodes and copper within polycyclic ligands may be effective for C_{2+} product formation.[113,120] Consider the CO_2RR selectivity of a series of phthalocyanine-based catalysts: PcCu–Cu–O, PcCo–Cu–O, Pc–Cu–O, Pc–Cu–NH, CuPc, and Cu-PPCOF. PcCu–Cu–O features two distinct copper sites – both with square planar geometry.

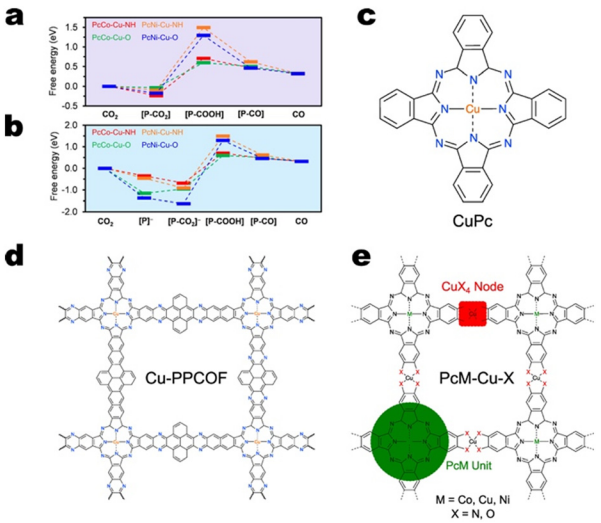

Fig. 9 Free energy diagrams for CO production on metallophthalocyanine-based Cu MOFs considering the a) concerted PCET mechanism and b) sequential PCET mechanism. Free energies are relative to desorbed CO_2. Adapted with permission from Meng *et al.*[118] Copyright 2020 American Chemical Society. The structures of c) molecular PcCu, d) Cu-PPCOF, and e) PcM–Cu–X.

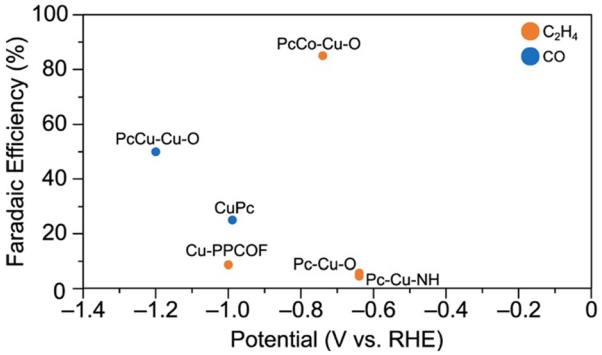

Fig. 10 Major CO_2RR product selectivity by metallophthalocyanine-based electrocatalysts. The data for PcCu–Cu–O are from Qiu *et al.*[113] The data for CuPc are from Kusama *et al.*[122] The data for PcCo–Cu–O, Pc–Cu–O, and Pc–Cu–NH are from Meng *et al.*[118] The data for Cu-PPCOF is from Zhang *et al.*[117] All data are reported for the conditions at which the highest single product FE is obtained.

One site resides within the SBU and features a copper ion coordinated by the oxygen atoms of two 2,3,9,10,16,17,23,24-octahydroxy-phthalo-cyaninato copper(II) ligands. The second copper site exists within the phthalocyanine (Pc) ligand. Here, the four pyrrolic nitrogens of phthalocyanine coordinate copper. If the copper within the ligand is replaced by cobalt, we obtain PcCo–Cu–O. If the cobalt within the ligand is removed, we obtain Pc–Cu–O. And if the oxygen atoms in the SBU are replaced with nitrogen atoms, we obtain Pc–Cu–NH. Copper phthalocyanine (CuPc) is essentially the ligand of PcCu–Cu–O. Finally, the covalent organic framework, Cu-PPCOF, also features copper within a polycyclic ligand, but instead of by a copper node, the phthalocyanine units are linked by pyrene units. The structures of the phthalocyanine-based catalysts are shown in Fig. 9c–e.

The major CO_2RR product faradaic efficiencies for each of these catalysts are compiled in Fig. 10. Firstly, while PcCu–Cu–O exhibits 50% $FE_{C_2H_4}$, PcCo–Cu–O exhibits primarily CO production (85% FE_{CO}). Pc–Cu–O and Pc–Cu–NH, which feature CuX_4 nodes but do not feature copper within polycyclic ligands, display poor CO_2RR performance (5.6% FE_{CO} and 4.5% FE_{CO}, respectively).[118] Cu-PPCOF also exhibits poor CO_2RR performance (8.6% FE_{CO}). Notably, CuPc does produce C_2H_4, albeit with lower selectivity (25% $FE_{C_2H_4}$). Together, these observations suggest that both copper sites within PcCu–Cu–O are essential for C_2H_4 production.

On the contrary, a study by Zhong *et al.* suggests that PcCu–Cu–O exhibits poor CO_2RR selectivity altogether. Only CO production (11% FE_{CO}) was observed in the same 0.1 M HCO_3 electrolyte. However, we note that the conductive additive used by Zhong *et al.* (CNTs) differs from that used by Qiu *et al.* (carbon black). Qiu *et al.* also tested the CO_2RR performance of CNTs and PcCu–Cu–O mixed with CNTs in their setup. Under identical conditions to the experiments with PcCu–Cu–O, CNTs exhibited 100% FE for HER. Further, PcCu–Cu–O mixed with CNTs exhibited ~90% FE_{HER} and ~10% FE_{CO}.[110] Thus, we contend that in the study by Zhong *et al.*, competition from the HER reduces C_{2+} product selectivity.

Given this explanation for the disparity reported in CO_2RR products selectivity for PcCu–Cu–O, C_2H_4 production by the related single-site catalyst, CuPc, supports the argument presented by Qiu *et al.*:[113] CO produced at the CuO_4 node migrates to the copper within phthalocyanine where it couples with adsorbed CO_2RR intermediates to yield C_2H_4.[113] These results suggest the feasibility of the dual-site design paradigm for Cu MOFs.

6.1.2. Atomic models of node-based SBUs. On a related note to our discussion on node-based Cu MOFs, we highlight the importance of the model used in theoretical calculations. Firstly, theoretical models on two-dimensional (2D) Cu MOFs generally only consider reaction on basal planes. However, without experimental evidence, one cannot eliminate the possible contribution of edge sites to Cu MOF reactivity. For 2D MOFs with AA stacking and small (<4 Å) interplanar distances, C–C coupling may be feasible on edge sites.[119]

Secondly, consider the implications of the calculations performed by Liu *et al.* to account for the differences in CH_4 production by Cu-DBC, Cu-HHTP, and Cu-THQ (Fig. 8a).[111] Note that since the same atomic model (Fig. 8c) is used for both Cu-HHTP and Cu-THQ, the calculations cannot possibly account for the fact that the CO selectivity exhibited by Cu-THQ is more than double that exhibited by Cu-HHTP. While this experimental observation may be attributed to bulk catalyst properties (*e.g.*, pore size) due to their effects on the active site (*e.g.*, local CO_2 concentration), the inability of the CuO_4 model to capture the differences in CO production suggests the importance of the ligand in tuning the electronic structure of the active site. This is underscored by

the fact that Cu-HATNA-MOF, another Cu MOF featuring a single CuO_4 node, exhibits greater CH_4 selectivity than Cu-DBC (78% *vs.* 56% FE_{CH_4}).[123]

Moreover, the importance of including the ligand can be seen when evaluating the C–C coupling mechanism proposed by Qiu and co-workers.[113] Note that stronger CO adsorption on the Pc unit compared to on the CuO_4 node supports the feasibility of the dual-site mechanism. The adsorption energies obtained by Qiu *et al.* are consistent with this requirement. On the contrary, DFT calculations performed by Zhang *et al.* suggest that CO is more stable on the CuO_4 node than on the phthalocyanine unit.[117]

Fig. 11 plots $E_{CuO_4} - E_{PcCu}$, the difference in CO adsorption energy on the CuO_4 node and the copper within the Pc unit, for each cluster model employed by Qiu *et al.*[113] and Zhang *et al.*[117] A negative value of $E_{CuO_4} - E_{PcCu}$ indicates stronger adsorption on the CuO_4 node. For adsorption on both the CuO_4 node and the Pc unit, the immediate coordination environment is identical for both studies. However, observe that Zhang *et al.* employed a model featuring a DBC ligand for adsorption on the CuO_4 node. Additionally, observe that their model for adsorption on the Pc unit is truncated with amine groups. The fact that only the ligands connected to the nodes differ suggests that changes away from the active site have a significant impact on the free energy of adsorbates. This point is further illustrated when comparing the CO_2RR and HER overpotentials on the SBUs of PcM–Cu–X MOFs (Fig. 12a and b). Calculated CO_2RR and HER overpotentials change by up to 0.43 eV and 0.19 eV, respectively, depending on the metal within the Pc unit. The upcoming section on ligand effects expands on the role that the ligand plays in modulating the reactivity of the SBU.

6.1.3. Cluster-based SBUs. The copper coordination environment in Cu MOFs can also be modified by incorporation of additional copper atoms within the SBU. HKUST-1, also known as $Cu_3(btc)_2$, is a well-known example of this paradigm. The SBU of HKUST-1 consists of a paddle-wheel cluster in which two copper atoms are coordinated by the oxygens of four benzene-1,3,5-tricarboxylate ligands. The copper dimer contains two square planar copper atoms separated 2.65 Å which lie in parallel planes (Fig. 13a).[124] Note that the coordination geometry of the copper atoms in HKUST-1 is similar to that of previously mentioned Cu MOFs with CuO_4 nodes, Cu-HHTP, Cu-THQ, and PcCu–Cu–O. Despite this similarity, HKUST-1 displays the ability to produce a wider range of CO_2RR products than any one of

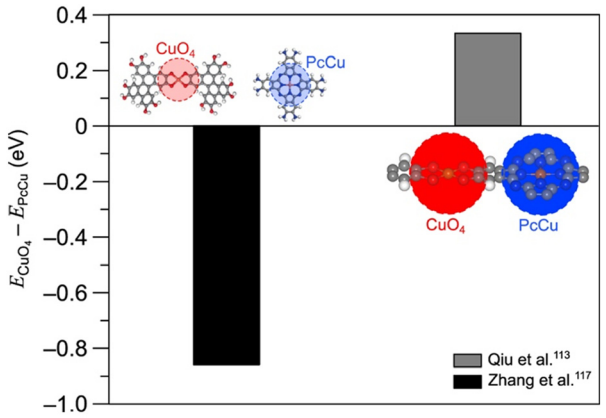

Fig. 11 Differences between CO adsorption energies on CuO_4 nodes and PcCu units as calculated by Zhang *et al.*[117] and Qiu *et al.*[113] Note that the energies by Zhang *et al.*[117] are calculated relative to CO_2 using the computational hydrogen electrode model,[24] and the energies by Qiu *et al.* are calculated relative to CO. For each set of calculations, the cluster models are displayed adjacent to the data point. In all atomic models, the red, grey, blue, orange, and white spheres denote oxygen, carbon, nitrogen, copper, and hydrogen atoms, respectively.

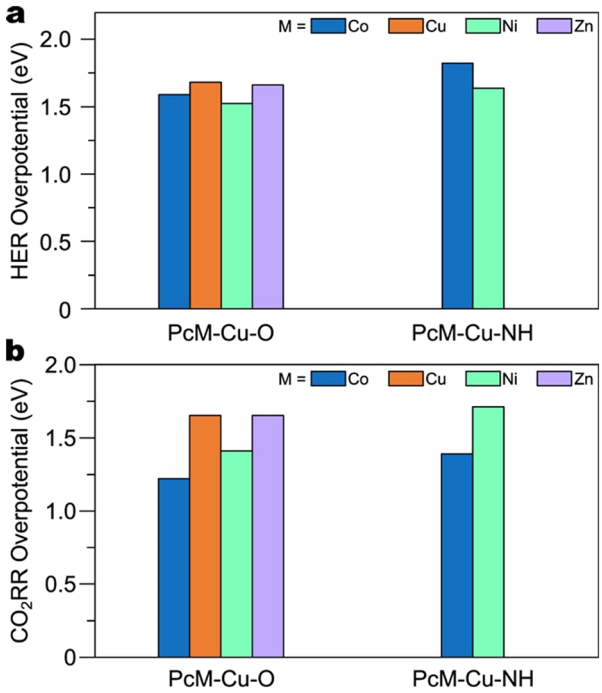

Fig. 12 DFT-calculated overpotentials for a) CO and b) H_2 production on the SBUs of various PcM–Cu–X MOFs. Data for Co- and Ni-bearing MOFs from Meng *et al.*[118] Data for PcCu–Cu–O and PcZn–Cu–O from Zhong *et al.*[121]

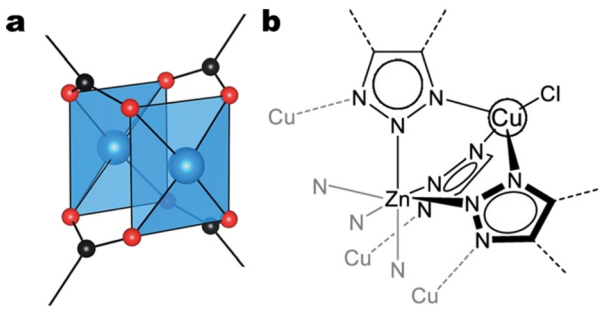

Fig. 13 a) Close-up of the copper dimer in the coordinatively unsaturated (anhydrous) structure of HKUST-1. The blue, red, and black spheres denote copper, oxygen, and carbon atoms, respectively. Adapted from Hendon & Walsh.[124] b) The local structure of the $\{Cu_4ZnCl_4\}^{6+}$ cluster, constituting the Cu_4^{II}-MFU-4l SBU. Adapted with permission from Zhu *et al.*[134] Copyright 2021 American Chemical Society.

these Cu MOFs. Under various reaction conditions and electrode geometries, HKUST-1 has been reported for alcohol,[125] hydrocarbon,[126–129] and organic acid production.[107] This ability to produce $>2e^-$ products extends to not only other MOFs with Cu dimers,[130–132] but also other Cu MOFs with cluster-based SBUs,[133,134] suggesting the importance of cluster-based SBUs for $>2e^-$ product formation. Fig. 14 compares node- and cluster-based Cu MOFs based on their selectivity for $>2e^-$ products. For a detailed account of $>2e^-$ product formation by Cu MOFs, we direct the reader to Table S2.† Evidently, the number of cluster-based Cu MOFs which yield $>2e^-$ products far exceed that of node-based Cu MOFs.

CO_2RR studies on Cu MOFs containing SBUs with more than two copper atoms are scarce. To the best of our knowledge, only three such studies exist.[133–135] Zhu *et al.* examined the CO_2RR performance of Cu_4^{II}-MFU-4l, a Cu MOF consisting of a $\{Cu_4ZnCl_4\}^{6+}$ cluster SBU and bis(1*H*-1,2,3-triazolo-[4,5-b],[4′,5′-*i*])dibenzo-[1,4]-dioxin (btdd) ligands.[134] The $\{Cu_4ZnCl_4\}^{6+}$ cluster can be visualized as four Cu^{2+} ions positioned at the corners of a tetrahedron featuring a single Zn^{2+} ion at its centroid. Further, the Zn^{2+} ion is octahedrally coordinated by six N atoms from six different btdd ligands, and each Cu^{2+} ion is tetrahedrally coordinated by three N atoms from three different btdd ligands and a single Cl^- ion. Each btdd unit is a hexadentate ligand, bridging two SBUs by coordinating two Cu^{2+} ions and one Zn^{2+} ion in each SBU. Fig. 13b illustrates the local structure of the $\{Cu_4ZnCl_4\}^{6+}$ cluster.

Under reaction conditions, the Cu^{2+} ions are reduced to Cu^+ ions, and the Cl^- ions are eliminated. The resulting CuN_3 active sites feature copper ions coordinated by three nitrogen atoms and one labile solvent H_2O molecule, effectively yielding Cu^+ ions with trigonal pyramidal geometries. The reduced catalyst with Cu^+ ions is referred to as Cu_4^I-MFU-4l and exhibits a maximum CH_4 selectivity of 92% at −1.2 V *vs.* RHE.

Based on *in situ* ATR-FTIR and DFT calculations, the authors contend that the observed CO_2RR selectivity and HER suppression derives from the stabilization of CO_2RR intermediates and destabilization of H_2O. The calculated equilibrium positions suggest more favourable interactions between CO_2RR intermediates and the active site than between H_2O and the active site. For *COOH, this is illustrated in Fig. 15a wherein *COOH is stabilized *via* an H-bonding interaction with an aromatic hydrogen. For *CHO and *CO, this is illustrated in Fig. 15b–d wherein the Cu–C distances between copper and the carbon atom on CO_2RR intermediates are shorter than the Cu–O distance between copper within the SBU and the oxygen atom in H_2O. *CHO and *CO are also stabilized *via* H-bonding interactions. Moreover, Zhu *et al.* reasoned that the aromatic hydrogens on the btdd ligand destabilize H_2O.

These effects manifest in the free energies of adsorbed CO_2RR intermediates relative to that of adsorbed H_2O

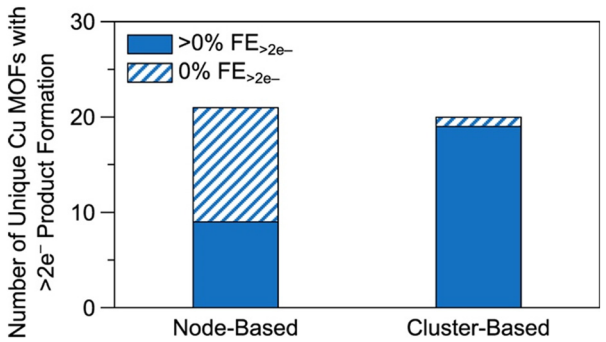

Fig. 14 Comparison of the number of unique node- and cluster-based Cu MOFs and Cu MOF composites. The solid regions denote the number of unique Cu MOFs reported with greater than 0% FE for $>2e^-$ products. The striped regions denote the number of unique Cu MOFs reported with 0% FE for $>2e^-$ products. Raw data available in Table S2.† For details on methodology, see the ESI.†

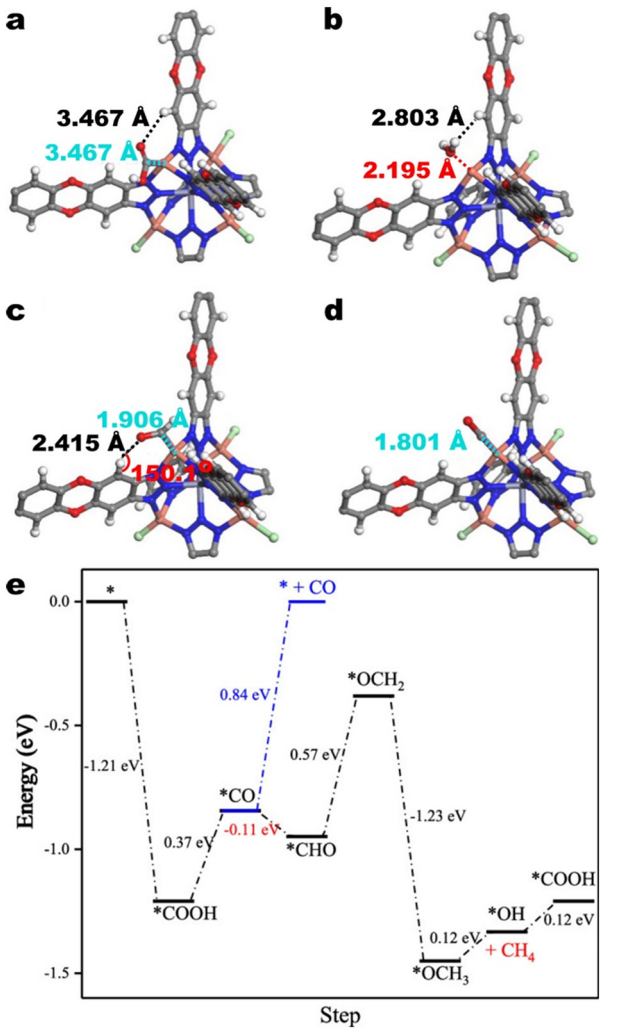

Fig. 15 Atomic scale models of the interactions of a) *COOH, b) *H_2O, c) *CHO, and d) *CO with a Cu atom in the SBU and aromatic hydrogens on the btdd ligand. The grey, white, red, green, blue, and orange spheres denote carbon, hydrogen, oxygen, chlorine, nitrogen, and copper atoms, respectively. e) Free energy diagram for CH_4 formation on Cu_4^I-MFU-4l. Adapted with permission from Zhu *et al.*[134] Copyright 2021 American Chemical Society.

(Fig. 15e). DFT calculations indicate that all detected CO_2RR intermediates are more stable than H_2O and that the selectivity for CH_4 over non-hydrogenated product CO stems from the thermodynamic barrier for CO desorption over *CO hydrogenation. In addition to H-bonding, the authors identify σ–π back bonding between Cu^+ and CO as a factor for the thermodynamic barrier for CO desorption.

The second study by van Phuc *et al.* investigates the CO_2-RR performance of a 2,5-dihydroxy-1,4-benzenedicarboxylate-based catalyst, Cu-MOF-74.[135] Cu-MOF-74 features helical Cu–O–C rods constructed from 6-coordinated Cu^{2+} centres. Each copper atom is coordinated by three carboxyl groups, two hydroxy groups, and a solvent molecule. The rods consist of edge-sharing CuO_6 octahedra and constitute the SBU (Fig. 16a).[136] It is interesting to note that unlike the vast majority of cluster-based Cu MOFs (Fig. 14), Cu-MOF-74 exhibits only CO production (85% FE_{CO}). As such, an investigation of the CO selectivity of Cu-MOF-74 may illuminate the design principles underlying $>2e^-$ CO_2RR.

Thirdly, we note the work of Dong *et al.* on NNU-50, which features a hexanuclear copper cluster SBU with strong cuprophilic interactions.[133] NNU-50 is comprised of $Cu_3(Me_4BPz)_{3/2}$ (Me_4BPz = 3,3′,5,5′-tetramethyl-4-4′-bipyrazolyl) clusters; adjacent clusters form a trigonal antiprism (Fig. 16b). Like many CO_2RR catalysts, NNU-50 switches selectivity from C_2H_4 (36% $FE_{C_2H_4}$ at −0.8 V *vs.* RHE) to CH_4 production (66.4% FE_{CH_4} −1.0 V *vs.* RHE) at more negative potentials. Further, NNU-50 maintains 61.4% FE_{CH_4} at total current densities of over 750 mA cm^{-2} (−1.2 V *vs.* RHE).[138]

The performance of Cu MOFs with multimetallic SBUs can also be modulated by reducing the extent to which the copper atoms are coordinated. Nam *et al.* showed that by thermally treating HKUST-1, the carboxylate moieties within the SBU sequentially detach, yielding further undercoordinated copper atoms.[137] As a result, they achieved 45% FE for ethylene compared to the less than 15% FE for ethylene obtained by untreated HKUST-1 under the same conditions. In the same vein, Wei *et al.* generated low coordination copper sites by creating oxygen vacancies in Cu-DBC *via* high energy O_2 plasma bombardment.[132] After ten minutes of plasma activation, the so-called PA-Cu-DBC-1 catalyst still retains its crystallinity and avoids formation of metallic copper. Notably, PA-Cu-DBC-1 exhibits higher selectivity for CH_4 (75.3%) than any other reported Cu-DBC catalyst in neutral conditions.[123,138] These two examples highlight the possibility that defect engineering, frequently employed in the design of pure metal catalysts but seldom employed in the design of Cu MOFs, may improve CO_2RR performance.

6.1.4. Final takeaways for SBU design. Node-based and cluster-based Cu MOFs show distinct CO_2RR capabilities. As shown in Fig. 14 and 17, Cu MOFs featuring cluster-based SBUs more frequently exhibit $>2e^-$ and C_{2+} selectivity than do Cu MOFs featuring node-based SBUs. Presumably, the superiority of cluster-based Cu MOFs over node-based Cu MOFs for C_{2+} derives from the existence of adjacent catalytic sites on which C–C coupling can occur. Nonetheless, the data suggests strategies for improving C_{2+} product formation on node-based Cu MOFs.

Firstly, as the separation between active sites is too large for C–C coupling to occur between adsorbed species, the combination of weakly binding CO-producing sites and strongly binding CO-coupling sites may enhance C_{2+} product formation. Secondly, observe that eight of the nine node-based Cu MOFs exhibiting $>2e^-$ product formation also exhibit C_{2+} product formation and that only one node-based Cu MOF (CR-MOF) produces HCOOH (Tables S2 and S3†). Circumstantially, this suggests C_{2+} product formation *via* a CO intermediate, implying that either CO adsorption or protonation is a descriptor for C_{2+} selectivity in node-based Cu MOFs. CO adsorption studies may illuminate the more suitable of the two explanations or signal difficulties in CO dimerization. In the case of PcM–Cu–O catalysts, it appears that weak CO adsorption is responsible for poor C_{2+} selectivity.[118,121]

Finally, it is unclear to what extent modifications away from the active site influence the electronic structure of copper within the active site. Although we emphasize the importance of copper's immediate coordination environment for the CO_2RR performance of MOFs, we note that ample

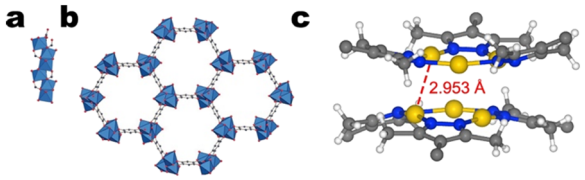

Fig. 16 Representation of a) the helical Cu–O–C rods and b) the crystalline framework of Cu-MOF-74 with the SBUs linked by 2,5-dihydroxy-1,4-benzenedicarboxylate ligands. Red and grey spheres denote oxygen and carbon atoms, respectively. Copper atoms are represented by blue octahedra. Hydrogens are omitted for clarity. Reproduced with permission from Rosi *et al.*[136] Copyright 2005 American Chemical Society. c) The hexanuclear cluster constituting the SBU of NNU-50. Yellow, blue, white, and grey spheres denote copper, nitrogen, hydrogen, and carbon atoms, respectively.

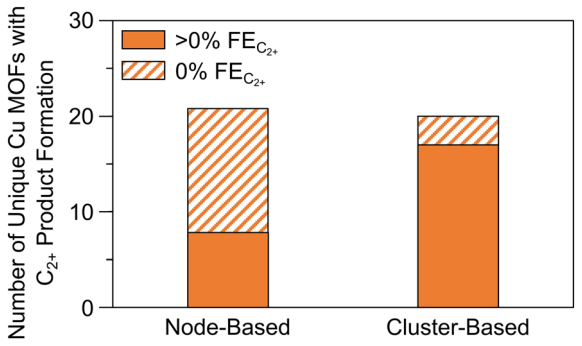

Fig. 17 Comparison of the number of unique node- and cluster-based Cu MOFs and Cu MOF composites. The solid regions denote the number of unique Cu MOFs reported with greater than 0% FE for C_{2+} products. The striped regions denote the number of unique Cu MOFs reported with 0% FE for C_{2+} products. Raw data available in Table S3.† For details on methodology, see the ESI.†

evidence suggests that the order at longer length scales plays a role as well. In several examples, a given MOF exhibits higher CO_2RR selectivity and/or activity than its molecular analogue (*e.g.*, PcCu–Cu–O and CuPc,[113] NNU-50 and Cu_6-MePz,[133] Cu_2(CuTCPP) and CuTCPP,[120] HATNA-Cu-MOF, $[(n\text{-}C_3H_7)_4N]_2[Cu(C_6Cl_4O_2)_2]$, and HATNA-6OH (ref. 123)). While this trend may be attributable to non-electronic effects, such as diffusion kinetics or catalyst surface area, we contend that the ligand may also modulate reactivity *via* the active site's electronic structure. That is, just as descriptors which account for second nearest neighbours (*viz.* the GCN) are insightful for transition metal catalysts, assessments of the relevant chemical environment for the active site of Cu MOFs may benefit from consideration of the ligand. Experimentally, Cu MOFs with the same CuO_4 SBU exhibit a wide range of CO_2RR reactivities. Moreover, theoretical calculations indicate that the chemical structure of the ligand affects the adsorption of intermediates on CuO_4 nodes. While it may be difficult to assess the electronic effect of the ligand directly, determining the scale of non-electronic effects may provide insight into the degree of electronic structure modulation by the ligand. The following section expands on the effect of the ligand on CO_2RR reactivity.

6.2. Ligand effects

The ligand is another major determinant of MOF properties. In addition to dictating the bulk structure, spacing of SBUs, and pore size, the ligand can host additional active sites for CO_2RR and influence the electrical properties of the MOF. Furthermore, chemical species within the ligand may indirectly affect the electronic structure of the copper atom within the SBU. In this section, we present observations on the effect of the ligand on CO_2RR by Cu MOFs. We specifically highlight correlations between CO_2RR performance and ligand substituent electronegativity, the presence of framework nitrogen atoms, ligand flexibility, and active site hydrophobicity.

6.2.1. Substitution within the ligand. The studies by Chen *et al.*[140] and Wang *et al.*[139] investigated the effect of substitution in a series of 1,4-benzene dicarboxylate-based MOFs featuring copper dimer SBUs. The series of MOFs, denoted as X–Cu-BDC (where X = NH_2, $2NH_2$, OH, 2OH, F, 2F, 2Cl, 2Br, or H), differ in the electron-withdrawing ability of the species occupying the 2 and 5 positions on the benzene within the ligand (Fig. 18a).

The study by Chen *et al.* indicates that electron-withdrawing groups correlate with higher selectivity and lower onset potentials toward C_{2+} products than do electron-donating groups.[140] The maximum faradaic efficiencies for C_{2+} products exhibited by 2F–Cu-BDC, F–Cu-BDC, Cu-BDC, OH-BDC, and NH_2–Cu-BDC are shown in Fig. 18b. Further, when the C_{2+} products partial current is normalized by CO_2 uptake, the trend is more pronounced. The C_{2+} product partial current density is two times greater than that of Cu-BDC and five times greater than that of NH_2–Cu-BDC.

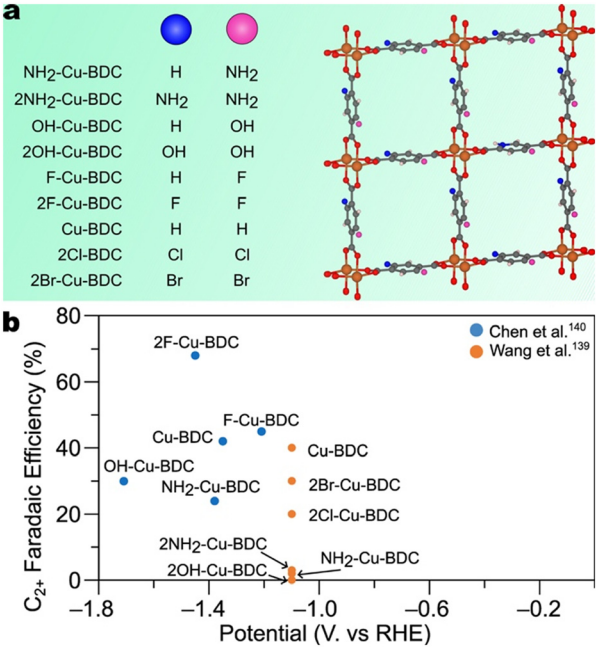

Fig. 18 a) Depiction of the general structure of the series of substituted 1,4-benzene dicarboxylate-based MOFs studied by Chen *et al.*[140] and Wang *et al.*[139] Grey, orange, red, and white spheres denote carbon, copper, oxygen, and hydrogen atoms. Pink and blue spheres denote variable functional groups. b) Faradaic efficiencies for C_{2+} products by X–Cu-BDC MOFs studied by Chen *et al.*[140] and Wang *et al.*[139]

Chen *et al.* suggest two competing effects upon substitution: H_2O dissociation and CO_2 adsorption.[140] The authors suggest that the electron-withdrawing ability of the substituted group correlates positively with the ease of H_2O dissociation, thereby increasing the local *H concentration, facilitating *CO hydrogenation to *CHO, and enhancing C–C coupling. Secondly, substitution of electron-donating groups resulted in higher CO_2 adsorption ability than did the substitution of electron-withdrawing groups. We note, however, that the trend observed by Chen *et al.* in alkaline conditions differs from that determined by Wang *et al.* in neutral conditions. Faradaic efficiencies reported by Wang *et al.* indicate that Cu-BDC exhibits higher C_{2+} selectivity than 2Cl–Cu-BDC, 2Br–Cu-BDC, NH_2–Cu-BDC, 2OH–Cu-BDC, and $2NH_2$–Cu-BDC.[139]

6.2.2. Nitrogen-containing ligands. HATNA-Cu-MOF, Cu-HHTQ, and Cu-HHTP feature hexagonally shaped pores and square planar CuO_4 nodes. HATNA-Cu-MOF and Cu-HHTQ feature hexahydroxyl-hexaazatrinaphthylene- and 2,3,7,8,12,13-hexahydroxytricycloquinazoline-based ligands, respectively. Cu-HHTP has been described previously. Fig. 19a–c depict all three MOFs. Investigations of the CO_2RR performance of these three Cu MOFs support the previously suggested link between ligand substituents and SBU reactivity. Specifically, the studies investigating CO_2RR performance in neutral conditions suggest the importance of nitrogen within the ligand for $>2e^-$ products.

HATNA-Cu-MOF exhibits 78% FE for CH_4 production,[123] and Cu-HHTQ exhibits 53.6% FE for CH_3OH production.[141]

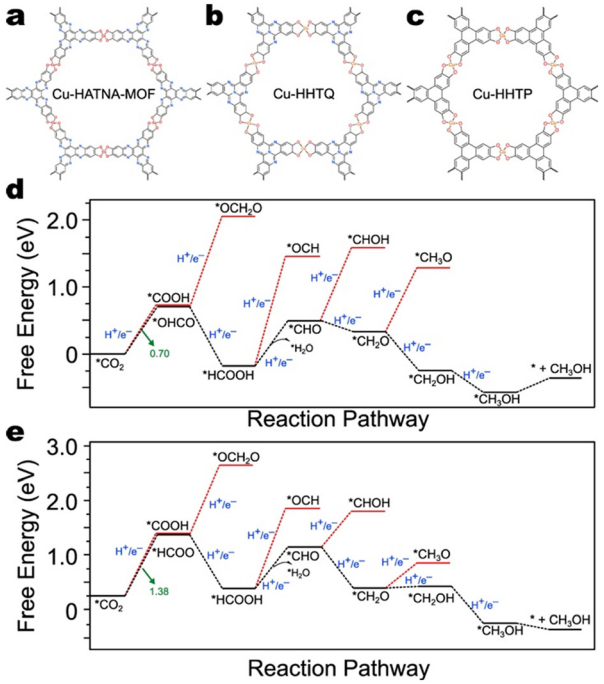

Fig. 19 The structures of a) HATNA-Cu-MOF,[123] b) Cu-HHTQ,[141] and c) Cu-HHTP.[117] Free energy diagrams for CH_3OH production by d) Cu-HHTQ and e) Cu-HHTP.[141] Data from Liu *et al.*[141]

However, the highest reported single-product faradaic efficiency exhibited by Cu-HHTP under similar conditions is for CO (50%).[113,118,141,142] There are no thorough DFT calculations to date studying the CO_2RR mechanism on HATNA-Cu-MOF; however, DFT calculations performed by Liu *et al.* explain the disparity in CO_2RR selectivity between Cu-HHTQ and Cu-HHTP (Fig. 19d and e).[141] Specifically, on Cu-HHTP, the free energy difference for the first PCET is 0.68 eV higher than it is on Cu-HHTQ. As both catalysts possess CuO_4 nodes, their results suggest that the ligands do, in fact, affect CO_2RR selectivity.

6.2.3. Active site flexibility. As a final case-study on the effect of the ligand, we highlight a study by Zhuo *et al.* investigating the correlation between ligand flexibility and C–C coupling ability in a set of metal azolate frameworks (MAFs).[131] Each MAF-2 analogue features a copper dimer within the SBU with a Cu–Cu distance of 3.4 Å, suggesting the potential for C–C coupling. Each copper atom is coordinated by three nitrogen atoms on three separate azolate ligands, and each ligand coordinates three copper atoms (Fig. 20a). Distinguished by their ligands, MAF-2ME (Fig. 20b), MAF-2E (Fig. 20c), and MAF-2P (Fig. 20d) feature methyl, ethyl, and propyl, side groups, respectively.

Zhuo *et al.* argue that by modifying the flexibility of groups adjacent to the active site, hydrocarbon production can be rationally tuned. The results indicate that as the ligand becomes bulkier, the selectivity switches from C_2H_4 to CH_4 production. Based on *in situ* ATR-FTIR measurements and DFT calculations (Fig. 20e–g), two competing effects are suggested: ligand flexibility/steric hindrance and ligand

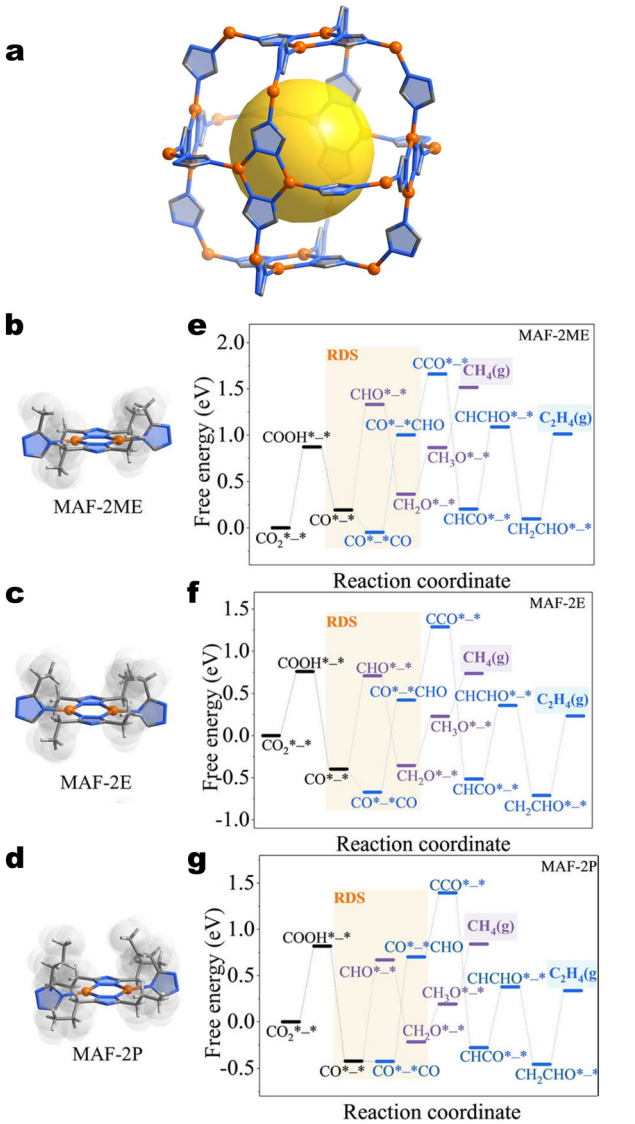

Fig. 20 Structures of MAF-2 analogues a) the Cu(I) triazolate backbone with ligand side groups omitted. Local coordination environments of b) MAF-2ME, c) MAF-2E, and d) MAF-2P. Orange spheres denote copper atoms. Blue, grey, and white edges denote nitrogen, carbon, and hydrogen atoms. Orange spheres denote copper atoms. Free energy diagrams for CH_4 and C_2H_4 formation on e) MAF-2ME, f) MAF-2E, and g) MAF-2P. Reproduced with permission from Zhuo *et al.*[131] Copyright 2022 John Wiley & Sons, Inc.

hydrophobicity. The authors argue that bulky groups within the ligand prevent the accommodation of multiple intermediates and inhibit C–C coupling. Simultaneously, the bulkier, more hydrophobic ligands inhibit HER. Accordingly, MAF-2P exhibited the highest selectivity for CH_4 (55.9% at −1.5 V *vs.* RHE), and MAF-2E exhibited the highest selectivity for C_2H_4 (51.2% at −1.3 V *vs.* RHE).

In summary, in addition to modulating CO_2 adsorption, ligand substituents may modulate hydrophobicity, H_2O dissociation, HER suppression and C–C coupling. The studies presented suggest that even when distant from the active site, ligand substituents affect the CO_2RR reactivity of Cu MOFs.

We continue to explore this theme in the following section in the context of active transition metals.

6.3. Inclusion of other transition metals

Although copper catalysts produce C_{2+} products, selectivity for a single CO_2RR product is poor.[30,41,76] On the other hand, other transition metals exhibit high selectivity, albeit for C_1 products, such as CO and HCOOH.[143] Since CO is an intermediate for C_{2+} products, one strategy to improve C_{2+} selectivity may be combining sites which produce CO with those that couple and reduce CO. In principle, one could tune the properties of the C–C coupling site without compromising the effectiveness of the CO-producing site. To this effect, the incorporation of active heteroatoms represents a strategy to design dual-site CO_2RR catalysts for C_{2+} product formation. This section presents insights relevant to the implementation of this strategy.

Firstly, we highlight the effect of incorporating cobalt, nickel, and zinc into metallophthalocyanine-based MOFs with square planar CuO_4 nodes. Note that while cobalt and zinc are typically known to produce CO, nickel is known to facilitate HER.[41,76,144] Studies indicate that the inclusion of these three metals into metallophthalocyanine-based Cu MOFs results exclusively in CO production. Cobalt results in the highest CO production (85% FE_{CO}),[113,118] followed by nickel (56% FE_{CO})[118] and then zinc (9% FE_{CO}).[121]

As mentioned earlier, PcCu–Cu–O and PcCu both facilitate C_{2+} product formation. Thus, the copper sites within phthalocyanines have been regarded as C–C coupling sites.[118,122] It stands to reason that replacing copper within the SBU of PcCu–Cu–O with a CO-producing metal, such as Zn, should improve C_{2+} product formation. However, the study by Zhong *et al.* indicates that the copper site of PcCu–Zn–O is not active for C_{2+} product formation, as PcCu–Zn–O only yields CO (88% FE_{CO}).[121] Although this result implies that the reactivity of the two sites in metallophthalocyanine-based Cu MOFs cannot be tuned independently, we note again that in this study, PcCu–Cu–O exhibited only CO production (11% FE_{CO}). Indeed, the electrodes employed in this study were prepared by mixing the Cu MOFs with CNTs, which may suppress C_{2+} product formation.[113] Nonetheless, DFT calculations support the notion that the SBU affects the reactivity of the Pc unit. Fig. 21a and b illustrate that the overpotentials for CO_2RR and HER on the Pc unit of phthalocyanine-based MOFs can be changed by up to 0.36 eV and 0.22 eV, respectively, by modifying the SBU. These results underscore the value of a follow-up study with a different conductive additive. By controlling for the conductive additive, such a study would provide a clearer comparison with which to evaluate of the generalizability of the dual-site paradigm illustrated by Qiu and co-workers.[113]

Alternatively, copper within the SBUs may be partially replaced by transition metals to yield multimetallic MOFs. One such example of this paradigm was reported in a study by van Phuc *et al.*, which featured a series of trimetallic Cu MOFs.[145] The MOFs are designed as isostructural to HKUST-1 and host two CO-producing metals, Pd and Zn, in addition to copper. We note, however, that characterizations indicate that the metals may exist in metallic form, and clear evidence for incorporation into the MOF structure was not observed.[145] These observations may account for the fact that the as-synthesized catalyst only exhibited selectivity for CO (95% FE_{CO}) whereas HKUST-1 typically exhibits C_{2+} selectivity.[107,125,126,128,137]

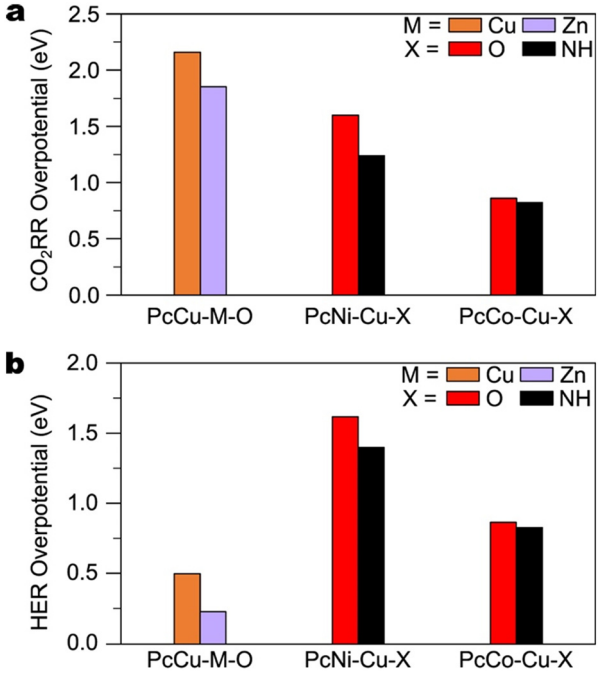

Fig. 21 DFT-calculated overpotentials for a) CO and b) H_2 production on the Pc units of various PcM_1–M_2–X MOFs. Data for Co- and Ni-bearing MOFs from Meng *et al.*[118] Data for PcCu–Cu–O and PcZn–Cu–O from Zhong *et al.*[121]

Transition metals may also be incorporated by simply physically mixing as-synthesized MOFs. Albo *et al.* prepared various bimetallic blends comprised of HKUST-1 and CAU-17, a bismuth-based MOF.[126] Under the conditions tested, CAU-17 does not produce alcohols, and pure HKUST-1 exhibits maximum faradaic efficiencies for CH_3OH and C_2H_5OH of about 3% and 10%, respectively. However, the optimal blend, CuBi12, consisting of 12% CAU-17, exhibited maximum MeOH and EtOH selectivities of 18.2% and 28.3%, respectively. This nonlinear enhancement of alcohol production suggests a synergistic effect of the two MOFs. The authors postulated that the enhanced production of alcohols by the MOF blends could be mainly ascribed to the formation of $HCOO^-$ at bismuth sites, which is then transferred to neighbouring copper active sites where further conversion toward alcohols takes place.

The incorporation of other transition metals offers flexibility in the design of Cu MOFs for CO_2RR. Novel selectivity may derive from changes to the local concentrations of intermediates or the electronic structure of

active sites. The design of dual-site Cu MOFs is a promising strategy to improve C_{2+} product selectivity; however, the electronic structure of the two active sites may be coupled, further complicating realization of this paradigm. Additional studies can illuminate the generalizability of this strategy and the potential synergy of multiple active sites. The next section examines synergistic effects between MOF and non-MOF phases.

6.4. Cu MOF composites

For several Cu MOFs, post-reaction characterizations indicate that the active catalyst may be a composite phase consisting of the Cu MOF and metallic aggregates. Such composite phases, herein denoted as Cu MOF composites, can also be derived from copper oxides. Fig. 22 depicts each of these paradigms for Cu MOF composite synthesis. In this section, we outline the potential advantages of and address issues with their implementation. We limit our scope to examples in which the Cu MOF is reportedly catalytically active and exclude reports of MOF pre-catalyst systems.

6.4.1. Cu MOF-derived composites. In CO_2RR conditions, copper within the SBU can be reduced to form a metallic copper or copper oxide phase. For example, studies report that Cu-HHTP forms Cu_2O nanoclusters exposing the $Cu_2O(111)$ facet[142] and that Cu-THQ forms copper nanoclusters exposing the Cu(111) facet.[146] Alternatively, as was illustrated for Cu-DBC, thermal treatment can give rise to a CuO nanoparticle-decorated MOF.[139]

Fig. 23 illustrates the potential of Cu MOF composites by comparing their CO_2RR selectivity to that of their constituents in the same experimental conditions. Whereas Cu-HHTP produces CO with a maximum selectivity of 20% in the same conditions, Cu_2O@Cu-HHTP exhibits 73% FE_{CH_4}.[142] Similarly, CuO@Cu-BDC exhibits 50% $FE_{C_2H_4}$ compared to 40% by Cu-BDC.[139] Cu_2O@Cu-HHTP, Cu(111)@Cu-THQ, and CuO@Cu-BDC also exhibit higher CO_2RR selectivities than their metal/metal-oxide constituents, Cu_2O, Cu, and CuO, respectively (Fig. 23).

Studies suggest that synergistic effects may arise from favourable interactions between exposed functional groups and intermediates[142] or dual-site functionality.[112] It is important to note, however, that the electrochemically constructed MOF composites lack stability. Additional facets and oxide phases are detectable at extended reaction times. Accordingly, unstable product selectivity and CO_2RR performance is observed. CuO@Cu-BDC exists as an exception, exhibiting both structural and CO_2RR performance stability in the conditions tested.[139]

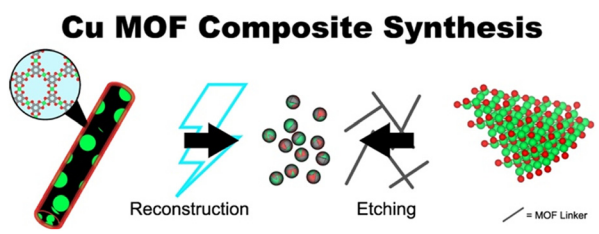

Fig. 22 Representative syntheses for Cu MOF composites. The left-hand side depicts the synthesis of Cu(111)@Cu-THQ *via* electrochemical reconstruction of Cu-THQ reported by Zhao *et al.*[146] The right-hand side depicts the synthesis of Cu_2O@Cu-MOF *via* etching for Cu_2O reported by Tan *et al.*[128] Green, red, and grey spheres denotes copper, oxygen, and carbon atoms, respectively.

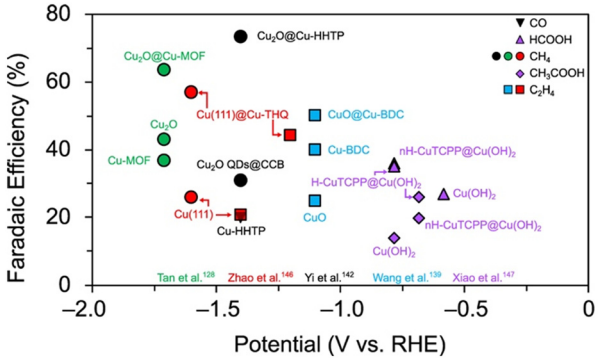

Fig. 23 Maximum faradaic efficiencies for CO, HCOOH, CH_4, CH_3COOH, and C_2H_4 production for various Cu MOF composites compared to that of their constituent metallic and Cu MOF catalysts in the same experimental setup. QDs = quantum dots. CCB = conductive carbon black.

6.4.2. Oxide-derived composites. The next paradigm of Cu MOF composite formation effectively operates in reverse, meaning that a Cu MOF phase is constructed from a non-MOF phase. One such example was demonstrated by Tan and co-workers. A Cu_2O-MOF core–shell composite was synthesized by partially etching Cu_2O nanospheres in the presence of benzene-1,3,5-tricarboyxlic acid to form a Cu MOF shell, resembling HKUST-1.[128] In identical conditions, the resulting composite, Cu_2O@Cu-MOF, exhibits higher CH_4 selectivity (63.2% FE_{CH_4}) than both Cu_2O and the pure Cu MOF phase (Fig. 23). The authors attribute this improved performance to better CO_2 adsorption relative to H_2O adsorption. We note that although the CO_2RR performance of Cu_2O@Cu-MOF was stable for up to six hours, metallic copper was detected after the reaction indicating reduction of the copper in the composite.

As a final example, we highlight the work by Xiao and co-workers. In this study, a Cu_2(CuTCPP) MOF phase was constructed from $Cu(OH)_2$ nanoarrays to yield helical, H-CuTCPP@$Cu(OH)_2$, and non-helical, nH-CuTCPP@$Cu(OH)_2$, nanocomposites. The Cu MOF phase features a copper atom within a porphyrin ligand and a copper dimer within the SBU. Both H-CuTCPP@$Cu(OH)_2$ and nH-CuTCPP@$Cu(OH)_2$ exhibit higher maximum selectivities for HCOOH (35% and 35%, respectively) and CH_3COOH (26.1% and 19.8%, respectively) than $Cu(OH)_2$ (27% FE_{HCOOH} and 14% FE_{CH_3COOH}) in the conditions tested (Fig. 23).[147]

The syntheses of MOF-derived composites can be regarded as instances of favourable MOF transformations. We have shown that such transformations can enhance CO_2RR performance such that the resultant composite catalyst

outperforms its constituent catalysts. Oftentimes, however, these composite catalysts appear to be intermediate phases formed under reaction conditions. As such, without further understanding of these transformations, the use of MOF composites as effective CO_2RR catalysts remains unreasonable. Also, note that despite reports of MOFs forming composites under CO_2RR conditions, several of these MOFs have been reported elsewhere without mention of the formation of a composite phase (ESI† file). This point underlines the importance of our following discussion, which more generally addresses the topic of *in situ* MOF transformations.

6.5. *In situ* transformations and Cu MOF stability

The long-term stability of Cu MOFs remains a significant roadblock to their adoption for CO_2RR. Significantly, Cu MOFs frequently exhibit decaying performance. Even when no performance drops are immediately obvious, Cu MOFs may undergo physical and chemical transformations. As such, studies elucidating the factors which dictate stability and govern degradation mechanisms are vital. Herein, we categorize the types of transformations observed for Cu MOFs in CO_2RR and highlight useful design strategies for promoting stability.

6.5.1. Classification of *in situ* transformations. Specifically, we delineate three categories for the transformations associated with CO_2RR conditions that are observed for Cu MOF electrodes. Firstly, the Cu MOF may undergo electrochemical reconstruction/degradation, yielding either a MOF-derived or metallic phase that persists when the electrode is unpolarized. Such transformations are characterizable by several *ex situ* methods after the reaction (*e.g.*, XRD, SEM, XPS).[148] Many of the Cu MOFs mentioned up to this point exhibit signs of such irreversible transformations under CO_2RR conditions (Table S1†). Despite this, the degradation processes of many MOFs remain insufficiently characterized. Although the properties of the resulting phase, such as the copper oxidation state or crystallinity, are occasionally reported, the mechanism and the factors which govern the mechanism require further investigation. As an outlier with respect to such studies, several in-depth investigations focus on HKUST-1. *In situ* and *operando* measurements indicate the formation of metallic nanoparticles and dendritic nanostructures under CO_2RR conditions.[129,149–151]

The second classification of transformation encompasses physical or chemical processes which may occur without electrode polarization, such as leaching of the catalyst into the electrolyte or inherent instability in the electrolyte. During this type of degradation, peeling off catalytic material from the electrode support may enhance HER due to easier access for H_2O, leading to lower CO_2RR selectivity.[126] Identification of this form of degradation may consist of electron microscopy or X-ray diffraction of the catalyst or spectroscopic analysis of the electrolyte.[148] The hydrolysis of HKUST-1 is a famous example for which there exists detailed investigation of the various stages of degradation.[151]

The final classification of transformation refers to reversible transformations which occur under CO_2RR conditions and are only discernible by *in situ* or *operando* techniques. These transformations are suggested by changes in oxidation states or coordination numbers and can be identified by surface characterization techniques such as AFM, XPS, or XAS.[148] For example, *operando* measurements by Majidi *et al.*, 2021 revealed that under CO_2RR conditions, copper is reduced to Cu^+ nanoclusters (and potentially metallic copper) but rapidly re-oxidizes when the system is returned to the open circuit voltage.[112] Studies suggest that the reversibility of copper reduction derives from the small size of copper particles formed *in situ*.[112,129]

In practice, a given MOF may undergo any combination of the above transformations. Nevertheless, stable Cu MOFs do exist, as some catalysts have been reported to exhibit unchanging performance with no evidence of a transformation for multiple hours (Table S1†). Based on these examples, we highlight a few strategies for designing stable Cu MOFs under CO_2RR conditions. Specifically, we focus on design strategies for preventing electrochemically induced transformations. For a comprehensive overview of the strategies for designing stable MOFs in aqueous conditions, in different pHs, under mechanical stress, and in the presence of various coordinating anions, we suggest the excellent review by Yuan and co-workers.[105]

Finally, note that the aforementioned transformations are not inherently undesirable. Often, the resulting material exhibits favourable CO_2RR performance.[152] In such a case, it is more appropriate to refer to the as-synthesized MOF as a precatalyst. The strategies presently described address the case in which one desires to preserve the order afforded by as-synthesized MOFs.

6.5.2. Strategies for designing stable Cu MOFs for CO_2RR. Firstly, in 2D Cu MOFs, π–π interactions between layers stabilize the MOF structure. In particular, larger π-conjugation planes and the presence of heteroatoms within the ligand backbone can enhance these interactions.[153] For example, Cu MOFs with smaller π-conjugation planes devoid of heteroatoms (*e.g.*, Cu-THQ[112] and Cu-HHTP[142]) are less stable than those possessing larger π-conjugation planes containing heteroatoms (*e.g.*, Cu-HHTQ,[141] HATNA-Cu-MOF,[123] and phthalocyanine-based Cu MOFs[113,118,121]). DFT calculations of the π–π stacking complexation energies of hexaazatrinaphthylene and triphenylene support this observation.[123] As a counterexample, we note that Cu_2(CuTCPP) undergoes electrochemical reconstruction in CO_2RR conditions.[130] However, the AB stacking pattern and out-of-plane benzenedicarboxylate linkers of Cu_2(CuTCPP) prevent efficient overlap of the π-systems of the porphyrin moieties which may account for the reduced stability of Cu_2(CuTCPP).

Strong intermolecular interactions can also stabilize copper within the SBU. For example, the strong cuprophilic interactions within the hexanuclear cluster of NNU-50 stabilize Cu^+ under CO_2RR conditions.[133] Additionally, Weng *et al.*

suggested that the metal ion–ligand binding affinity of a copper complex influences the threshold potential as well as the reversibility of the reductive demetallation process. They also proposed that the restructuring process may involve other important factors such as the solubility of the demetallated ligand and the electronic structure of the complex.[129] However, note that the presence of open metal sites is important for the catalytic activity of metal centres,[154] The redox activity of the metal within the SBU contributes to MOF conductivity through charge-hopping transport mechanisms.[103,155]

Finally, as copper is often reduced to Cu^+ under CO_2RR conditions,[94,150,156,157] coordination geometries preferred by Cu^+, such as the tetrahedral geometry, may prevent demetallation.[131,134] A notable example of this is Cu_4^{II}-MFU-4l[134] in which the three nitrogen atoms and one Cl^- ion form a tetrahedron around the copper ions within the SBU. Again, one should consider the existence of open metal sites when diverging from square planar copper coordination geometries.

7. Challenges & perspectives

In this review, we have focused on the aspects of copper-based MOF design that can be linked to selectivity in electrochemical carbon dioxide reduction. Several trends have emerged. Secondary building units featuring copper clusters commonly produce C_{2+} products. On the other hand, solitary, square planar nodes, frequently produce CO or HCOOH while other node-based Cu MOFs yield CO, HCOOH, and $>2e^-$ products. Regarding ligand design, modifications away from the SBU can significantly affect product selectivity. The incorporation of catalytic metal centres within the ligand can facilitate C–C coupling. Such catalysts show promise as a design paradigm for increasing C_{2+} product selectivity. Further, studies suggest that the reactivity of Cu MOFs can be tuned *via* adjacent functional groups and may be affected by more distant modifications. This point is especially relevant for computational work. Finally, the instability of Cu MOFs can be leveraged to yield CO_2RR active MOF composites. As illustrated in Fig. 24, however, it is more often the case that such transformations represent one of several challenges to be addressed.

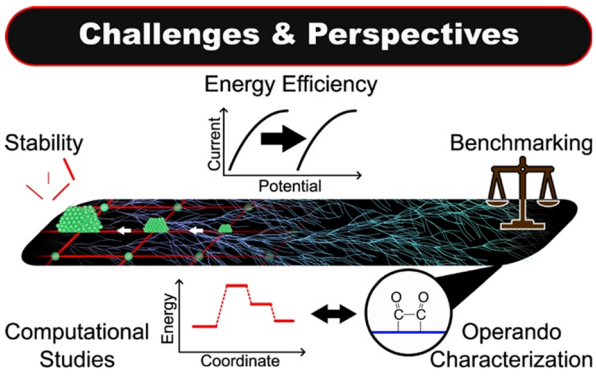

Fig. 24 An illustration of the key challenges and perspectives for the development of copper-based metal–organic frameworks for CO_2RR.

1) The instability of copper-based metal–organic frameworks severely limits their application for industrial scale electrochemical carbon dioxide reduction. Atomic-scale design may improve the resilience of Cu MOFs to electrochemical degradation by stabilizing copper units and limiting nanocluster formation. The application of electrode synthesis techniques such as spray-drying or electrodeposition may aid in preserving the physical integrity of Cu MOF electrodes. In part, a fundamental understanding of instability motivates the next challenge.

2) The dynamic nature of Cu MOFs during CO_2RR demands that their properties are characterized at operating conditions. We highlight the importance of *in situ* and *operando* methods, such as ATR-FTIR, SEIRA, DRIFTS, XPS, and XAS, which can illuminate how Cu MOF properties, as they manifest under CO_2RR conditions, affect catalyst performance. Particularly, we note that such characterizations are prerequisite for probing electronic properties of copper, such as the proportions of Cu^0, Cu^+, and Cu^{2+} species, and for addressing the aforementioned challenge of stability. That the Cu^{2+} ion is reduced at more positive potentials than required for CO_2RR highlights the relevance of the copper oxidation state. Regarding stability, we note that the time scales on which reconstruction or decomposition take place may prohibit their detection by implicit means such as chronoamperometry or *ex situ* characterizations.[148] It should not be assumed that stable CO_2RR performance implies a stable catalyst or that the structure of the catalyst after reaction is that of the catalyst during reaction. These assumptions can lead to incorrect characterizations of Cu MOF stability.

3) It is also important to understand the CO_2RR mechanisms of Cu MOFs. Hence, the combination of theoretical and experimental studies will continue to play an important role in the development of the field. Density functional theory calculations can provide evidence for a proposed reaction mechanism and insight into how a given Cu MOF facilitates CO_2RR selectivity. *In situ* and *operando* characterizations can provide experimental evidence for reaction intermediates as well as an accurate representation of the active site during CO_2RR. This is especially important for theoretical calculations, the efficacy of which is predicated on reasonable atomic models.

We also emphasize the importance of using standard calculation conventions to determine the thermodynamics of CO_2RR reaction mechanisms. Namely, we note that although adsorption energies of intermediates often mirror reactivity trends, these trends may diverge for intermediates of significantly different size, polarity, or binding atom. Proposed reaction mechanisms should be based on Gibbs free energy calculations, and the free energy of several potential intermediates for a given step should be compared to determine the minimum energy path for the reaction mechanism.

Further, that CO_2RR mechanisms exhibit strong pH/potential-dependencies suggests that simple thermochemical

models may be inadequate or unreliable. Considering this, one may need to employ more sophisticated models which account for solvation[32,36,158–162] or the potential-dependence of transition states.[32,33,37,73,144,158,163] For CO_2RR on transition metals, the use of such models has yielded results which more closely align with experiment.[37,144,164] However, to the best of our knowledge, only two works studying CO_2RR on Cu MOFs have employed such methods.[118,119]

4) The energy efficiency of Cu MOFs must be improved through increases in activity and selectivity. Firstly, Cu MOFs still require large overpotentials for valuable products, and the activities reported for Cu MOFs are comparatively lower than those reported for state-of-the-art CO_2RR catalysts. Although the selectivities of Cu MOFs are comparable to state-of-the-art catalysts, since Cu MOFs exhibit potential-dependent selectivity, valuable product yields cannot be increased by simply increasing the overpotential. As such, increasing the intrinsic activity of active sites is a priority. Notably, it appears that improving intrinsic activity may be a significant challenge.[100]

That the conductivities of Cu MOFs are low also poses a problem. In the case that conducting binders must be used, we note that care should be taken to control for the HER activity of the binder. As discussed in this review, CNTs may suppress C_{2+} selectivity.[121]

5) Finally, we emphasize the importance of benchmarking and current density reporting procedures. Frequently, publications do not include benchmarking data for their experimental setup. As such, it is impossible to deconvolve differences in performance due to the catalyst from variations in experimental setups. To facilitate meaningful comparisons of CO_2RR performance, authors should report the performance of a standard CO_2RR catalyst, such as copper foil, in their experimental setup. In the same vein, current densities are typically reported with respect to geometric surface area. However, ECSA-normalized current densities are more insightful for comparing the intrinsic activity of catalysts. Analysis of this metric in conjunction with others, such as CO_2 adsorption capacity, may then elucidate design principles for increasing the intrinsic activity of Cu MOFs.

Adoption of the conventions may also aid in rationalizing the observation that the same Cu MOF may be reported as exhibiting large variations in CO_2RR performance (activity and selectivity) under similar reported experimental conditions. For example, across the four studies which report CO_2RR by Cu-HHTP in neutrally buffered H-cells, maximum CO selectivity varies from 0% to 50% faradaic efficiency.[113,118,141,142] Similarly, in the two studies which report CO_2RR by Cu-DBC in neutrally buffered H-cells, maximum CH_4 selectivity varies from 10% to 34% faradaic efficiency.[123,132]

Nonetheless, the flexibility in design afforded by copper-based metal–organic frameworks makes them attractive as platforms for electrochemical carbon dioxide reduction. Further work is needed to understand the role of solvent, improve catalyst stability, and increase valuable product selectivity. The integrated design of Cu MOFs at the atomic scale and reaction conditions at the macroscale can potentially improve the CO_2RR performance of Cu MOFs. Moreover, the modular nature of Cu MOFs lends itself to machine learning applications.[165,166] With continued development, Cu MOFs may provide a solution to the challenge of C_{2+} selectivity in CO_2RR.

Conflicts of interest

There are no conflicts to declare.

Acknowledgements

The authors acknowledge the support received from the National Research Council of Canada's Materials for Clean Fuels (MCF) Challenge R&D Program (Grant number CH-MCF-115-1). This research in part was enabled by the support from the University of Calgary's Canada First Research Excellence Fund Program, the Global Research Initiative in Sustainable Low Carbon Unconventional Resources. UN acknowledges the support from Alberta Graduate Scholarship.

References

1 Z. Sun, Y. Hu, D. Zhou, M. Sun, S. Wang and W. Chen, *ACS Energy Lett.*, 2021, **6**, 3992–4022.
2 M. Gattrell, N. Gupta and A. Co, *J. Electroanal. Chem.*, 2006, **594**, 1–19.
3 Y. Wang, J. Liu, G. Zheng, Y. Wang, J. Liu and G. Zheng, *Adv. Mater.*, 2021, **33**, 2005798.
4 G. Zhang, L. Li, Z.-J. Zhao, T. Wang and J. Gong, *Acc. Mater. Res.*, 2023, **4**, 212–222.
5 S. Nitopi, E. Bertheussen, S. B. Scott, X. Liu, A. K. Engstfeld, S. Horch, B. Seger, I. E. L. Stephens, K. Chan, C. Hahn, J. K. Nørskov, T. F. Jaramillo and I. Chorkendorff, *Chem. Rev.*, 2019, **119**, 7610–7672.
6 D. Raciti and C. Wang, *ACS Energy Lett.*, 2018, **3**, 1545–1556.
7 Q. Zhou, W. Zhang, M. Qiu and Y. Yu, *Mater. Today Phys.*, 2021, **20**, 100443.
8 C. Zhu, S. Zhao, G. Shi and L. Zhang, *ChemSusChem*, 2022, **2022**, e202200068.
9 H. J. Peng, M. T. Tang, J. Halldin Stenlid, X. Liu and F. Abild-Pedersen, *Nat. Commun.*, 2022, **13**, 1–11.
10 Y. Zheng, A. Vasileff, X. Zhou, Y. Jiao, M. Jaroniec and S. Z. Qiao, *J. Am. Chem. Soc.*, 2019, **141**, 7646–7659.
11 F. N. Al-Rowaili, A. Jamal, M. S. Ba Shammakh and A. Rana, *ACS Sustainable Chem. Eng.*, 2018, **6**, 15895–15914.
12 R. Wang, F. Kapteijn and J. Gascon, *Chem. – Asian J.*, 2019, **14**, 3452–3461.
13 H. He, J. A. Perman, G. Zhu and S. Ma, *Small*, 2016, **12**, 6309–6324.
14 Y. Zhao, L. Zheng, D. Jiang, W. Xia, X. Xu, Y. Yamauchi, J. Ge, J. Tang, Y. Zhao, L. Zheng, D. Jiang, W. Xia, J. Ge, J. Tang, X. Xu and Y. Yamauchi, *Small*, 2021, **17**, 2006590.
15 Q. Wang, Y. Zhang, H. Lin and J. Zhu, *Chem. – Eur. J.*, 2019, **25**, 14026–14035.

16 D. Narváez-Celada and A. S. Varela, *J. Mater. Chem. A*, 2022, **10**, 5899–5917.
17 C. Wang, Z. Lv, W. Yang, X. Feng and B. Wang, *Chem. Soc. Rev.*, 2023, **52**, 1382–1427.
18 P. Friedlingstein, M. O'Sullivan, M. W. Jones, R. M. Andrew, L. Gregor, J. Hauck, C. le Quéré, I. T. Luijkx, A. Olsen, G. P. Peters, W. Peters, J. Pongratz, C. Schwingshackl, S. Sitch, J. G. Canadell, P. Ciais, R. B. Jackson, S. R. Alin, R. Alkama, A. Arneth, V. K. Arora, N. R. Bates, M. Becker, N. Bellouin, H. C. Bittig, L. Bopp, F. Chevallier, L. P. Chini, M. Cronin, W. Evans, S. Falk, R. A. Feely, T. Gasser, M. Gehlen, T. Gkritzalis, L. Gloege, G. Grassi, N. Gruber, Ö. Gürses, I. Harris, M. Hefner, R. A. Houghton, G. C. Hurtt, Y. Iida, T. Ilyina, A. K. Jain, A. Jersild, K. Kadono, E. Kato, D. Kennedy, K. Klein Goldewijk, J. Knauer, J. I. Korsbakken, P. Landschützer, N. Lefèvre, K. Lindsay, J. Liu, Z. Liu, G. Marland, N. Mayot, M. J. McGrath, N. Metzl, N. M. Monacci, D. R. Munro, S.-I. Nakaoka, Y. Niwa, K. O'Brien, T. Ono, P. I. Palmer, N. Pan, D. Pierrot, K. Pocock, B. Poulter, L. Resplandy, E. Robertson, C. Rödenbeck, C. Rodriguez, T. M. Rosan, J. Schwinger, R. Séférian, J. D. Shutler, I. Skjelvan, T. Steinhoff, Q. Sun, A. J. Sutton, C. Sweeney, S. Takao, T. Tanhua, P. P. Tans, X. Tian, H. Tian, B. Tilbrook, H. Tsujino, F. Tubiello, G. R. van der Werf, A. P. Walker, R. Wanninkhof, C. Whitehead, A. Willstrand Wranne, R. Wright, W. Yuan, C. Yue, X. Yue, S. Zaehle, J. Zeng and B. Zheng, *Earth Syst. Sci. Data*, 2022, **14**, 4811–4900.
19 V. UNFCCC, *Conference of the Parties to the United Nations Framework Convention on Climate Change*, 2015, pp. 1–32.
20 *IPCC, 2022: Climate Change 2022: Mitigation of Climate Change. Contribution of Working Group III to the Sixth Assessment Report of the Intergovernmental Panel on Climate Change*, ed. P. R. Shukla, J. Skea, R. Slade, A. al Khourdajie, R. van Diemen, D. McCollum, M. Pathak, S. Some, P. Vyas, R. Fradera, M. Belkacemi, A. Hasija, G. Lisboa, S. Luz and J. Malley, Cambridge University Press, Cambridge, UK, 2022.
21 P. Linstorm, *J. Phys. Chem. Ref. Data, Monogr.*, 1998, **9**, 1–1951.
22 S. Verma, B. Kim, H. R. M. Jhong, S. Ma and P. J. A. Kenis, *ChemSusChem*, 2016, **9**, 1972–1979.
23 O. S. Bushuyev, P. De Luna, C. T. Dinh, L. Tao, G. Saur, J. van de Lagemaat, S. O. Kelley and E. H. Sargent, *Joule*, 2018, **2**, 825–832.
24 J. K. Nørskov, J. Rossmeisl, A. Logadottir, L. Lindqvist, J. R. Kitchin, T. Bligaard and H. Jónsson, *J. Phys. Chem. B*, 2004, **108**, 17886–17892.
25 H. Eyring, *J. Chem. Phys.*, 1935, **3**, 107.
26 A. A. Peterson and J. K. Nørskov, *J. Phys. Chem. Lett.*, 2012, **3**, 251–258.
27 W. Deng, P. Zhang, B. Seger and J. Gong, *Nat. Commun.*, 2022, **13**, 1–9.
28 D. W. DeWulf, T. Jin and A. J. Bard, *J. Electrochem. Soc.*, 1989, **136**, 1686–1691.
29 K. J. P. Schouten, Y. Kwon, C. J. M. van der Ham, Z. Qin and M. T. M. Koper, *Chem. Sci.*, 2011, **2**, 1902–1909.
30 Y. Hori, A. Murata and R. Takahashi, *J. Chem. Soc., Faraday Trans. 1*, 1989, **85**, 2309–2326.
31 R. L. Cook, R. C. MacDuff and A. F. Sammells, *J. Electrochem. Soc.*, 1989, **136**, 1982–1984.
32 H. Xiao, T. Cheng, W. A. Goddard and R. Sundararaman, *J. Am. Chem. Soc.*, 2016, **138**, 483–486.
33 X. Liu, J. Xiao, H. Peng, X. Hong, K. Chan and J. K. Nørskov, *Nat. Commun.*, 2017, **8**, 1–7.
34 A. A. Peterson, F. Abild-Pedersen, F. Studt, J. Rossmeisl and J. K. Nørskov, *Energy Environ. Sci.*, 2010, **3**, 1311–1315.
35 P. Hirunsit, W. Soodsawang and J. Limtrakul, *J. Phys. Chem. C*, 2015, **119**, 8238–8249.
36 W. Luo, X. Nie, M. J. Janik and A. Asthagiri, *ACS Catal.*, 2016, **6**, 219–229.
37 X. Nie, M. R. Esopi, M. J. Janik and A. Asthagiri, *Angew. Chem., Int. Ed.*, 2013, **52**, 2459–2462.
38 A. Bagger, W. Ju, A. S. Varela, P. Strasser and J. Rossmeisl, *ChemPhysChem*, 2017, **18**, 3266–3273.
39 F. Calle-Vallejo and M. T. M. Koper, *Angew. Chem., Int. Ed.*, 2013, **52**, 7282–7285.
40 J. H. Montoya, C. Shi, K. Chan and J. K. Nørskov, *J. Phys. Chem. Lett.*, 2015, **6**, 2032–2037.
41 Y. Hori, in *Modern Aspects of Electrochemistry*, Springer, New York, 2008, pp. 89–189.
42 K. J. P. Schouten, Z. Qin, E. P. Gallent and M. T. M. Koper, *J. Am. Chem. Soc.*, 2012, **134**, 9864–9867.
43 K. J. P. Schouten, E. Pérez Gallent and M. T. M. Koper, *ACS Catal.*, 2013, **3**, 1292–1295.
44 J. H. Montoya, A. A. Peterson and J. K. Nørskov, *ChemCatChem*, 2013, **5**, 737–742.
45 R. B. Sandberg, J. H. Montoya, K. Chan and J. K. Nørskov, *Surf. Sci.*, 2016, **654**, 56–62.
46 J. D. Goodpaster, A. T. Bell and M. Head-Gordon, *J. Phys. Chem. Lett.*, 2016, **7**, 1471–1477.
47 E. E. Benson, C. P. Kubiak, A. J. Sathrum and J. M. Smieja, *Chem. Soc. Rev.*, 2008, **38**, 89–99.
48 H. Wan, Y. Jiao, A. Bagger and J. Rossmeisl, *ACS Catal.*, 2020, **11**, 533–541.
49 K. Zhao and X. Quan, *ACS Catal.*, 2021, **11**, 2076–2097.
50 A. Vasileff, Y. Zheng and S. Z. Qiao, *Adv. Energy Mater.*, 2017, **7**, 1700759.
51 Q. Lu, J. Rosen and F. Jiao, *ChemCatChem*, 2015, **7**, 38–47.
52 D. Johnson, Z. Qiao and A. Djire, *ACS Appl. Energy Mater.*, 2021, **4**, 8661–8684.
53 S. Siahrostami, *Ind. Eng. Chem. Res.*, 2018, **58**, 879–885.
54 Y. Cheng, S. Yang, P. Jiang, S. Wang, Y. Cheng, S. Wang, S. P. Jiang and S. Yang, *Small Methods*, 2019, **3**, 1800440.
55 J. He, N. J. J. Johnson, A. Huang and C. P. Berlinguette, *ChemSusChem*, 2018, **11**, 48–57.
56 A. Vasileff, C. Xu, Y. Jiao, Y. Zheng and S. Z. Qiao, *Chem*, 2018, **4**, 1809–1831.
57 J. Christophe, T. Doneux and C. Buess-Herman, *Electrocatalysis*, 2012, **3**, 139–146.
58 C. Yang, S. Li, Z. Zhang, H. Wang, H. Liu, F. Jiao, Z. Guo, X. Zhang and W. Hu, *Small*, 2020, **16**, 2001847.
59 Y. Y. Birdja, E. Pérez-Gallent, M. C. Figueiredo, A. J. Göttle, F. Calle-Vallejo and M. T. M. Koper, *Nat. Energy*, 2019, **4**, 732–745.

60 M. Golam Kibria, J. P. Edwards, C. M. Gabardo, C.-T. Dinh, A. Seifitokaldani, D. Sinton, E. H. Sargent, M. G. Kibria, C. Dinh, A. Seifitokaldani, E. H. Sargent, J. P. Edwards, C. M. Gabardo and D. Sinton, *Adv. Mater.*, 2019, **31**, 1807166.
61 J. Li, Y. Zhang and N. Kornienko, *New J. Chem.*, 2020, **44**, 4246–4252.
62 S. N. Steinmann, C. Michel, R. Schwiedernoch and P. Sautet, *Phys. Chem. Chem. Phys.*, 2015, **17**, 13949–13963.
63 J. Wang, H. Y. Tan, Y. Zhu, H. Chu and H. M. Chen, *Angew. Chem., Int. Ed.*, 2021, **60**, 17254–17267.
64 D. Gao, R. M. Arán-Ais, H. S. Jeon and B. Roldan Cuenya, *Nat. Catal.*, 2019, **2**, 198–210.
65 M. Li, H. Wang, W. Luo, P. C. Sherrell, J. Chen, J. Yang, M. H. Li, H. F. Wang, W. Luo, J. P. Yang, P. C. Sherrell and J. Chen, *Adv. Mater.*, 2020, **32**, 2001848.
66 Q. Zhang, J. Guan, Q. Zhang and J. Guan, *Adv. Funct. Mater.*, 2020, **30**, 2000768.
67 M. T. Darby, M. Stamatakis, A. Michaelides and E. C. H. Sykes, *J. Phys. Chem. Lett.*, 2018, **9**, 5636–5646.
68 Y. Hori, A. Murata and Y. Yoshinami, *J. Chem. Soc., Faraday Trans.*, 1991, **87**, 125–128.
69 I. Takahashi, O. Koga, N. Hoshi and Y. Hori, *J. Electroanal. Chem.*, 2002, **533**, 135–143.
70 Y. Hori, I. Takahashi, O. Koga and N. Hoshi, *J. Mol. Catal. A: Chem.*, 2003, **199**, 39–47.
71 Y. Hori, H. Wakebe, T. Tsukamoto and O. Koga, *Surf. Sci.*, 1995, **335**, 258–263.
72 Y. Huang, A. D. Handoko, P. Hirunsit and B. S. Yeo, *ACS Catal.*, 2017, **7**, 1749–1756.
73 J. Hussain, H. Jónsson and E. Skúlason, *ACS Catal.*, 2018, **8**, 5240–5249.
74 P. Sabatier, *Ber. Dtsch. Chem. Ges.*, 1911, **44**, 1984–2001.
75 K. P. Kuhl, T. Hatsukade, E. R. Cave, D. N. Abram, J. Kibsgaard and T. F. Jaramillo, *J. Am. Chem. Soc.*, 2014, **136**, 14107–14113.
76 K. P. Kuhl, E. R. Cave, D. N. Abram and T. F. Jaramillo, *Energy Environ. Sci.*, 2012, **5**, 7050–7059.
77 A. Xu, N. Govindarajan, G. Kastlunger, S. Vijay and K. Chan, *Acc. Chem. Res.*, 2022, **55**, 495–503.
78 K. W. Frese, in *Electrochemical and Electrocatalytic Reactions of Carbon Dioxide*, Elsevier, 1993, pp. 145–216.
79 C. Hahn, T. Hatsukade, Y. G. Kim, A. Vailionis, J. H. Baricuatro, D. C. Higgins, S. A. Nitopi, M. P. Soriaga and T. F. Jaramillo, *Proc. Natl. Acad. Sci. U. S. A.*, 2017, **114**, 5918–5923.
80 F. Calle-Vallejo, J. Tymoczko, V. Colic, Q. H. Vu, M. D. Pohl, K. Morgenstern, D. Loffreda, P. Sautet, W. Schuhmann and A. S. Bandarenka, *Science*, 2015, **350**, 185–189.
81 H. Mistry, A. S. Varela, S. Kühl, P. Strasser and B. R. Cuenya, *Nat. Rev. Mater.*, 2016, **1**, 1–14.
82 T. Cheng, H. Xiao and W. A. Goddard, *J. Am. Chem. Soc.*, 2017, **139**, 11642–11645.
83 C. S. Chen, A. D. Handoko, J. H. Wan, L. Ma, D. Ren and B. S. Yeo, *Catal. Sci. Technol.*, 2014, **5**, 161–168.
84 F. S. Roberts, K. P. Kuhl and A. Nilsson, *Angew. Chem.*, 2015, **127**, 5268–5271.
85 G. L. de Gregorio, T. Burdyny, A. Loiudice, P. Iyengar, W. A. Smith and R. Buonsanti, *ACS Catal.*, 2020, **10**, 4854–4862.
86 P. Hirunsit, *J. Phys. Chem. C*, 2013, **117**, 8262–8268.
87 D. Kim, J. Resasco, Y. Yu, A. M. Asiri and P. Yang, *Nat. Commun.*, 2014, **5**, 1–8.
88 M. Watanabe, M. Shibata, A. Kato, M. Azuma and T. Sakata, *J. Electrochem. Soc.*, 1991, **138**, 3382–3389.
89 Y. Zhou, F. Che, M. Liu, C. Zou, Z. Liang, P. de Luna, H. Yuan, J. Li, Z. Wang, H. Xie, H. Li, P. Chen, E. Bladt, R. Quintero-Bermudez, T. K. Sham, S. Bals, J. Hofkens, D. Sinton, G. Chen and E. H. Sargent, *Nat. Chem.*, 2018, **10**, 974–980.
90 S. Lee, G. Park and J. Lee, *ACS Catal.*, 2017, **7**, 8594–8604.
91 D. Ren, B. S. H. Ang and B. S. Yeo, *ACS Catal.*, 2016, **6**, 8239–8247.
92 E. L. Clark, C. Hahn, T. F. Jaramillo and A. T. Bell, *J. Am. Chem. Soc.*, 2017, **139**, 15848–15857.
93 D. Higgins, A. T. Landers, Y. Ji, S. Nitopi, C. G. Morales-Guio, L. Wang, K. Chan, C. Hahn and T. F. Jaramillo, *ACS Energy Lett.*, 2018, **3**, 2947–2955.
94 W. Zhang, P. He, C. Wang, T. Ding, T. Chen, X. Liu, L. Cao, T. Huang, X. Shen, O. A. Usoltsev, A. L. Bugaev, Y. Lin and T. Yao, *J. Mater. Chem. A*, 2020, **8**, 25970–25977.
95 M. Favaro, H. Xiao, T. Cheng, W. A. Goddard and E. J. Crumlin, *Proc. Natl. Acad. Sci. U. S. A.*, 2017, **114**, 6706–6711.
96 W. Ma, S. Xie, T. Liu, Q. Fan, J. Ye, F. Sun, Z. Jiang, Q. Zhang, J. Cheng and Y. Wang, *Nat. Catal.*, 2020, **3**, 478–487.
97 C.-T. Dinh, T. Burdyny, M. G. Kibria, A. Seifitokaldani, C. M. Gabardo, F. P. García de Arquer, A. Kiani, J. P. Edwards, P. de Luna, O. S. Bushuyev, C. Zou, R. Quintero-Bermudez, Y. Pang, D. Sinton and E. H. Sargent, *Science*, 2018, **360**, 783–787.
98 M. Luo, Z. Wang, Y. C. Li, J. Li, F. Li, Y. Lum, D. H. Nam, B. Chen, J. Wicks, A. Xu, T. Zhuang, W. R. Leow, X. Wang, C. T. Dinh, Y. Wang, Y. Wang, D. Sinton and E. H. Sargent, *Nat. Commun.*, 2019, **10**, 1–7.
99 F. Li, A. Thevenon, A. Rosas-Hernández, Z. Wang, Y. Li, C. M. Gabardo, A. Ozden, C. T. Dinh, J. Li, Y. Wang, J. P. Edwards, Y. Xu, C. McCallum, L. Tao, Z. Q. Liang, M. Luo, X. Wang, H. Li, C. P. O'Brien, C. S. Tan, D. H. Nam, R. Quintero-Bermudez, T. T. Zhuang, Y. C. Li, Z. Han, R. D. Britt, D. Sinton, T. Agapie, J. C. Peters and E. H. Sargent, *Nature*, 2019, **577**, 509–513.
100 O. Christensen, S. Zhao, Z. Sun, A. Bagger, J. V. Lauritsen, S. U. Pedersen, K. Daasbjerg and J. Rossmeisl, *ACS Catal.*, 2022, 15737–15749.
101 T. R. Cook, Y. R. Zheng and P. J. Stang, *Chem. Rev.*, 2013, **113**, 734–777.
102 Y. Wen, X. Wu and Q. Zhu, in *Advanced Structural Chemistry*, Wiley, 2021, pp. 283–389.
103 L. S. Xie, G. Skorupskii and M. Dincă, *Chem. Rev.*, 2020, **120**, 8536–8580.
104 Q. He, F. Zhan, H. Wang, W. Xu, H. Wang and L. Chen, *Mater. Today Sustain.*, 2022, **17**, 100104.
105 S. Yuan, L. Feng, K. Wang, J. Pang, M. Bosch, C. Lollar, Y. Sun, J. Qin, X. Yang, P. Zhang, Q. Wang, L. Zou, Y. Zhang,

L. Zhang, Y. Fang, J. Li, H.-C. Zhou, S. Yuan, L. Feng, K. Wang, J. Pang, M. Bosch, C. Lollar, Y. Sun, J. Qin, X. Yang, P. Zhang, Q. Wang, L. Zou, Y. Zhang, L. Zhang, Y. Fang, J. Li and H. Zhou, *Adv. Mater.*, 2018, **30**, 1704303.

106 R. Hinogami, S. Yotsuhashi, M. Deguchi, Y. Zenitani, H. Hashiba and Y. Yamada, *ECS Electrochem. Lett.*, 2012, **1**, H17.

107 R. Senthil Kumar, S. Senthil Kumar and M. Anbu Kulandainathan, *Electrochem. Commun.*, 2012, **25**, 70–73.

108 F. Calle-Vallejo, J. I. Martínez, J. M. García-Lastra, P. Sautet, D. Loffreda, F. Calle-Vallejo, P. Sautet, D. Loffreda and J. I. Martínez, *Angew. Chem.*, 2014, **126**, 8456–8459.

109 Z. Zhao, Z. Chen, X. Zhang and G. Lu, *J. Phys. Chem. C*, 2016, **120**, 28125–28130.

110 Ü. Kökçam-Demir, A. Goldman, L. Esrafili, M. Gharib, A. Morsali, O. Weingart and C. Janiak, *Chem. Soc. Rev.*, 2020, **49**, 2751–2798.

111 Y.-Y. Liu, H.-L. Zhu, Z.-H. Zhao, N.-Y. Huang, P.-Q. Liao and X.-M. Chen, *ACS Catal.*, 2022, **12**, 2749–2755.

112 L. Majidi, A. Ahmadiparidari, N. Shan, S. N. Misal, K. Kumar, Z. Huang, S. Rastegar, Z. Hemmat, X. Zou, P. Zapol, J. Cabana, L. A. Curtiss, A. Salehi-Khojin, L. Majidi, A. Ahmadiparidari, S. N. Misal, S. Rastegar, Z. Hemmat, A. Salehi-Khojin, N. Shan, P. Zapol, L. A. Curtiss, K. Kumar, J. Cabana, Z. Huang and X. Zou, *Adv. Mater.*, 2021, **33**, 2004393.

113 X. F. Qiu, H. L. Zhu, J. R. Huang, P. Q. Liao and X. M. Chen, *J. Am. Chem. Soc.*, 2021, **143**, 7242–7246.

114 J. Chatt and L. A. Duncanson, *J. Chem. Soc.*, 1953, 2939–2947.

115 J. S. Dewar, *Bull. Soc. Chim. Fr.*, 1951, **18**, C71–C79.

116 M. Loipersberger, Y. Mao and M. Head-Gordon, *J. Chem. Theory Comput.*, 2020, **16**, 1073–1089.

117 Y. Zhang, L. Z. Dong, S. Li, X. Huang, J. N. Chang, J. H. Wang, J. Zhou, S. L. Li and Y. Q. Lan, *Nat. Commun.*, 2021, **12**, 1–9.

118 Z. Meng, J. Luo, W. Li and K. A. Mirica, *J. Am. Chem. Soc.*, 2020, **142**, 21656–21669.

119 Z. H. Zhao, H. L. Zhu, J. R. Huang, P. Q. Liao and X. M. Chen, *ACS Catal.*, 2022, **12**, 7986–7993.

120 Y. Zhou, S. Chen, S. Xi, Z. Wang, P. Deng, F. Yang, Y. Han, Y. Pang and B. Y. Xia, *Cell Rep. Phys. Sci.*, 2020, **1**, 100182.

121 H. Zhong, M. Ghorbani-Asl, K. H. Ly, J. Zhang, J. Ge, M. Wang, Z. Liao, D. Makarov, E. Zschech, E. Brunner, I. M. Weidinger, J. Zhang, A. V. Krasheninnikov, S. Kaskel, R. Dong and X. Feng, *Nat. Commun.*, 2020, **11**, 1–10.

122 S. Kusama, T. Saito, H. Hashiba, A. Sakai and S. Yotsuhashi, *ACS Catal.*, 2017, **7**, 8382–8385.

123 Y. Liu, S. Li, L. Dai, J. Li, J. Lv, Z. Zhu, A. Yin, P. Li and B. Wang, *Angew. Chem., Int. Ed.*, 2021, **60**, 16409–16415.

124 C. H. Hendon and A. Walsh, *Chem. Sci.*, 2015, **6**, 3674–3683.

125 J. Albo, D. Vallejo, G. Beobide, O. Castillo, P. Castaño and A. Irabien, *ChemSusChem*, 2017, **10**, 1100–1109.

126 J. Albo, M. Perfecto-Irigaray, G. Beobide and A. Irabien, *J. CO2 Util.*, 2019, **33**, 157–165.

127 Y.-L. Qiu, H.-X. Zhong, T.-T. Zhang, W.-B. Xu, P.-P. Su, X.-F. Li and H.-M. Zhang, *ACS Appl. Mater. Interfaces*, 2018, **10**, 2480–2489.

128 X. Tan, C. Yu, C. Zhao, H. Huang, X. Yao, X. Han, W. Guo, S. Cui, H. Huang and J. Qiu, *ACS Appl. Mater. Interfaces*, 2019, **11**, 9904–9910.

129 Z. Weng, Y. Wu, M. Wang, J. Jiang, K. Yang, S. Huo, X. F. Wang, Q. Ma, G. W. Brudvig, V. S. Batista, Y. Liang, Z. Feng and H. Wang, *Nat. Commun.*, 2018, **9**, 1–9.

130 J. X. Wu, S. Z. Hou, X. da Zhang, M. Xu, H. F. Yang, P. S. Cao and Z. Y. Gu, *Chem. Sci.*, 2019, **10**, 2199–2205.

131 L. L. Zhuo, P. Chen, K. Zheng, X. W. Zhang, J. X. Wu, D. Y. Lin, S. Y. Liu, Z. S. Wang, J. Y. Liu, D. D. Zhou and J. P. Zhang, *Angew. Chem., Int. Ed.*, 2022, **61**, e202204967.

132 S. Wei, X. Jiang, C. He, S. Wang, Q. Hu, X. Chai, X. Ren, H. Yang and C. He, *J. Mater. Chem. A*, 2022, **10**, 6187–6192.

133 L. Z. Dong, Y. F. Lu, R. Wang, J. Zhou, Y. Zhang, L. Zhang, J. Liu, S. L. Li and Y. Q. Lan, *Nano Res.*, 2022, **15**, 10185–10193.

134 H. L. Zhu, J. R. Huang, X. W. Zhang, C. Wang, N. Y. Huang, P. Q. Liao and X. M. Chen, *ACS Catal.*, 2021, **11**, 11786–11792.

135 T. Van Phuc, S. G. Kang, J. S. Chung and S. H. Hur, *Mater. Res. Bull.*, 2021, **138**, 111228.

136 N. L. Rosi, J. Kim, M. Eddaoudi, B. Chen, M. O'Keeffe and O. M. Yaghi, *J. Am. Chem. Soc.*, 2005, **127**, 1504–1518.

137 D. H. Nam, O. S. Bushuyev, J. Li, P. De Luna, A. Seifitokaldani, C. T. Dinh, F. P. García De Arquer, Y. Wang, Z. Liang, A. H. Proppe, C. S. Tan, P. Todorović, O. Shekhah, C. M. Gabardo, J. W. Jo, J. Choi, M. J. Choi, S. W. Baek, J. Kim, D. Sinton, S. O. Kelley, M. Eddaoudi and E. H. Sargent, *J. Am. Chem. Soc.*, 2018, **140**, 11378–11386.

138 X. Zhou, J. Dong, Y. Zhu, L. Liu, Y. Jiao, H. Li, Y. Han, K. Davey, Q. Xu, Y. Zheng and S. Z. Qiao, *J. Am. Chem. Soc.*, 2021, **143**, 6681–6690.

139 L. Wang, X. Li, L. Hao, S. Hong, A. W. Robertson and Z. Sun, *Chin. J. Catal.*, 2022, **43**, 1049–1057.

140 R. Chen, L. Cheng, J. Liu, Y. Wang, W. Ge, C. Xiao, H. Jiang, Y. Li and C. Li, *Small*, 2022, 2200720.

141 J. Liu, D. Yang, Y. Zhou, G. Zhang, G. Xing, Y. Liu, Y. Ma, O. Terasaki, S. Yang and L. Chen, *Angew. Chem., Int. Ed.*, 2021, **60**, 14473–14479.

142 J. D. Yi, R. Xie, Z. L. Xie, G. L. Chai, T. F. Liu, R. P. Chen, Y. B. Huang and R. Cao, *Angew. Chem., Int. Ed.*, 2020, **59**, 23641–23648.

143 P. De Luna, C. Hahn, D. Higgins, S. A. Jaffer, T. F. Jaramillo and E. H. Sargent, *Science*, 2019, **364**, eaav3506.

144 J. Hussain, E. Skúlason and H. Jónsson, *Procedia Comput. Sci.*, 2015, **51**, 1865–1871.

145 T. Van Phuc, J. S. Chung and S. H. Hur, *Catalysts*, 2021, **11**, 537.

146 Z. H. Zhao, K. Zheng, N. Y. Huang, H. L. Zhu, J. R. Huang, P. Q. Liao and X. M. Chen, *Chem. Commun.*, 2021, **57**, 12764–12767.

147 Y. H. Xiao, Y. X. Zhang, R. Zhai, Z. G. Gu and J. Zhang, *Sci. China Mater.*, 2021, **65**, 1269–1275.

148 W. Zheng and L. Y. S. Lee, *ACS Energy Lett.*, 2021, **6**, 2838–2843.
149 W. Zhang, C. Huang, J. Zhu, Q. Zhou, R. Yu, Y. Wang, P. An, J. Zhang, M. Qiu, L. Zhou, L. Mai, Z. Yi and Y. Yu, *Angew. Chem., Int. Ed.*, 2022, **61**, e202112116.
150 L. Braglia, F. Tavani, S. Mauri, R. Edla, D. Krizmancic, A. Tofoni, V. Colombo, P. D'Angelo and P. Torelli, *J. Phys. Chem. Lett.*, 2021, **12**, 9182–9187.
151 M. Todaro, G. Buscarino, L. Sciortino, A. Alessi, F. Messina, M. Taddei, M. Ranocchiari, M. Cannas and F. M. Gelardi, *J. Phys. Chem. C*, 2016, **120**, 12879–12889.
152 Y. Zhou, R. Abazari, J. Chen, M. Tahir, A. Kumar, R. R. Ikreedeegh, E. Rani, H. Singh and A. M. Kirillov, *Coord. Chem. Rev.*, 2022, **451**, 214264.
153 J. H. Dou, M. Q. Arguilla, Y. Luo, J. Li, W. Zhang, L. Sun, J. L. Mancuso, L. Yang, T. Chen, L. R. Parent, G. Skorupskii, N. J. Libretto, C. Sun, M. C. Yang, P. V. Dip, E. J. Brignole, J. T. Miller, J. Kong, C. H. Hendon, J. Sun and M. Dincă, *Nat. Mater.*, 2020, **20**, 222–228.
154 A. Corma, H. García and F. X. Llabrés I Xamena, *Chem. Rev.*, 2010, **110**, 4606–4655.
155 L. Sun, M. G. Campbell and M. Dincă, *Angew. Chem., Int. Ed.*, 2016, **55**, 3566–3579.
156 S. H. Lee, J. C. Lin, M. Farmand, A. T. Landers, J. T. Feaster, J. E. Avilés Acosta, J. W. Beeman, Y. Ye, J. Yano, A. Mehta, R. C. Davis, T. F. Jaramillo, C. Hahn and W. S. Drisdell, *J. Am. Chem. Soc.*, 2021, **143**, 588–592.
157 A. D. Handoko, F. Wei, J. Lim, B. S. Yeo and Z. W. Seh, *Nat. Catal.*, 2018, **1**, 922–934.
158 X. Nie, W. Luo, M. J. Janik and A. Asthagiri, *J. Catal.*, 2014, **312**, 108–122.
159 M. Fishman, H. L. Zhuang, K. Mathew, W. Dirschka and R. G. Hennig, *Phys. Rev. B: Condens. Matter*, 2013, **87**, 245402.
160 K. Mathew, V. S. C. Kolluru, S. Mula, S. N. Steinmann and R. G. Hennig, *J. Chem. Phys.*, 2019, **151**, 234101.
161 K. Mathew, R. Sundararaman, K. Letchworth-Weaver, T. A. Arias and R. G. Hennig, *J. Chem. Phys.*, 2014, **140**, 084106.
162 T. Cheng, H. Xiao and W. A. Goddard, *Proc. Natl. Acad. Sci. U. S. A.*, 2017, **114**, 1795–1800.
163 J. Hussain, H. Jónsson and E. Skúlason, *Faraday Discuss.*, 2017, **195**, 619–636.
164 W. J. Durand, A. A. Peterson, F. Studt, F. Abild-Pedersen and J. K. Nørskov, *Surf. Sci.*, 2011, **605**, 1354–1359.
165 X. Wan, Z. Zhang, H. Niu, Y. Yin, C. Kuai, J. Wang, C. Shao and Y. Guo, *J. Phys. Chem. Lett.*, 2021, **12**, 6111–6118.
166 S. Siahrostami, S. R. Stoyanov, S. Gusarov, I. D. Gates and M. Karamad, in *Accelerated materials discovery: How to use Artificial Intelligence to speed up development*, ed. P. De Luna, De Gruyter, Berlin, 2022, pp. 27–64.